

Study of spin-dependent thermal transport and thermoelectric effects across ferromagnetic/nonmagnetic metal hybrid nanostructures

アサム, ナガルジュナ

<https://hdl.handle.net/2324/2236022>

出版情報 : 九州大学, 2018, 博士 (理学), 課程博士
バージョン :
権利関係 :

Study of spin-dependent thermal
transport and thermoelectric effects
across ferromagnetic/nonmagnetic
metal hybrid nanostructures

Nagarjuna Asam

March 2019

I dedicate this thesis to all those who write legibly
without jargon, obfuscation, forced passive voice and times new roman.

Abstract

Spin-caloritronics is a recent branch of spintronics where the interaction between heat and spin is studied. While the discovery of spin Seebeck effect and thermal spin injection show a promise towards heat-to-spin conversion, manipulation of spin current while using heat is also a possibility. With the experimental demonstration of Spin-dependent Seebeck effect, spin-dependent Peltier effect, thermal Hall effects, anomalous Nernst effect, a lot of new interesting physics has come into limelight. Going forward, both development of new device geometries and clear understanding of the physics in the existing devices is equally important. Particularly, there is a need to think beyond heat-to-spin-energy conversion alone. In this context, we studied a few other ways in which heat can interact with spin, leading to some new findings. In particular, we experimentally verified thermal analogues of three different spintronic effects.

First, we investigated the effect of a thermal gradient across a FM/NM/FM trilayer on the dynamics. By using the simple Joule heating from a W heater and measuring the Ferromagnetic Resonance (FMR) using Vector Network Analyzer (VNA), we systematically studied the dynamics under thermal spin injection caused by the thermal gradient. Here, beside the well-known damping-like spin transfer torque, we found new evidence for a field-like torque, resulting in a shift in the FMR frequency. Further, we found that the effect is pronounced when the top layer has smaller FMR dots instead of a large film, thereby showing a new way to improve spin injection efficiency by altering the geometry.

The above experiment has current-perpendicular-to-plane geometry. Keeping in mind that the current-in-plane geometry is easier to fabricate, we proceeded to study the effect of temperature gradient in-plane along the FM/NM/FM trilayer. By using orthogonal Pt wires as both heater and thermometer, we studied the flow of heat current along the trilayer nanowire. We found that the heat current also shows a giant magnetoresistance (GMR) like effect very similar to that of the widely used electrical version.

While analyzing the above, a distinct problem that we encountered is that a multitude of thermoelectric and thermal phenomena come into picture simultaneously complicating the analysis. Keeping this in mind, we attempted to find further evidence for the co-existence of multiple thermoelectric effects. We took the well-studied nonlocal geometry of the thermal spin injection device and found that a part of the detected signal upon thermal spin injection has been left unexplained until now. Upon taking a closer look, we showed that the anomalous thermal Hall effect also comes into play simultaneously with the anomalous Nernst effect apart from the dominant thermal spin-dependent Seebeck effect.

In summary, various effects of temperature gradient across a FM/NM/FM trilayer, along a FM/NM/FM trilayer and a FM/NM interface in a non-local spin valve geometry have been shown. As a result, regarding dynamics, evidence for field-like and damping-like spin transfer torque and regarding heat flow, a thermal version of the GMR effect were shown. Additionally, in

the non-local spin injection devices, simultaneous co-existence of anomalous Nernst effect, spin dependent Seebeck effect and anomalous thermal Hall was shown. In effect, experimental evidence for thermal spin transfer torque, thermal GMR and anomalous thermal Hall effect was found.

Contents

1	Introduction	7
1.1	Introduction and motivation	7
1.2	Outline of chapters	10
2	Theory and background	12
2.1	Introduction	12
2.2	Spin-independent electron transport	12
2.3	Electrical and thermal transport	13
2.3.1	Thermo-electric effects	15
2.4	Spin-dependent electron transport	17
2.4.1	Anisotropic Magnetoresistance	18
2.4.2	GMR	18
2.4.3	Hall effects	20
2.5	Magnetization dynamics	22
2.5.1	Ferromagnetic resonance	23
2.5.2	Spin-transfer torque	25
3	Fabrication and measurement methods	28

<i>CONTENTS</i>	2
3.1 Fabrication steps	29
3.1.1 Lithography	29
3.1.2 Deposition	30
3.2 Measurement methods	33
3.2.1 Vector Network Analyzer - Ferromagnetic Resonance .	33
3.2.2 Field-dependent lock-in measurement	36
4 Experiment 1: Thermally driven spin transfer torque	38
4.1 Introduction	38
4.2 Sample structure	40
4.3 Experiment details	44
4.4 Results and Discussion	47
4.4.1 Dependence on dot-size	55
4.5 Summary	55
5 Experiment 2: Thermal Spin valve effect	56
5.1 Introduction	56
5.2 Sample structure	57
5.3 Experiment details	60
5.4 Results and Discussion	61
5.4.1 NiFe/Cu/NiFe	61
5.4.2 Co/Cu/Co	65
5.5 Summary	69
6 Experiment 3: Anomalous thermal Hall effect	70
6.1 Introduction	70
6.2 Sample structure	72

<i>CONTENTS</i>	3
6.3 Measurement	74
6.4 Results and discussion	75
6.4.1 Upon reversing the roles of injector and detector	78
6.5 Summary	81
7 Summary	82

List of Figures

2.1	Peltier effect	15
2.2	Seebeck effect	16
2.3	GMR in perpendicular-to-plane configuration	19
2.4	Hall effect	20
2.5	Anomalous Hall effect	21
2.6	Magnetization dynamics under external magnetic field	23
2.7	Magnetization dynamics under spin transfer torque	26
3.1	Joule evaporation/triple source e-beam evaporation setup	31
3.2	DC/RF Sputter machine with several sources out of which we used Pt and W for the following experiments	32
3.3	RF Sputter machine for SiO ₂	34
3.4	Vector Network Analyzer setup	35
3.5	Lock-in measurement setup	36
4.1	A schematic of the device	41
4.2	Side view of the layers and their thickness	42
4.3	Fabrications steps	43
4.4	SEM image of the the device	44

4.5	Typical signal measured by VNA and corresponding multi-peak fitting	45
4.6	Typical signal measured by VNA and corresponding multi-peak fitting	46
4.7	Comsol simulation showing the temperature gradient across CoFeAl/Cu/NiFe trilayer in the inset	48
4.8	Heater current vs VNA signal	50
4.9	Heater current vs VNA signal zoomed in to NiFe peak	51
4.10	Parabolic fit of change in linewidth and frequency vs heater current	52
4.11	Heater current vs frequency shift for various NiFe dot sizes. We can see that smaller dots are causing better spin injection	53
4.12	A qualitative explanation of dot size dependence of spin injection efficiency. Apart from the spin current that is directly coming from below, NiFe dots also absorb a current from a radius of spin diffusion length in Cu around them.	54
5.1	A schematic of the device	58
5.2	Fabrication steps	59
5.3	Electrical GMR of NiFe/Cu/NiFe	61
5.4	Seebeck Voltage at Pt2 of NiFe/Cu/NiFe device showing thermal GMR	62
5.5	Result of COMSOL simulation showing a significant increase in the temperature	63
5.6	Results of COMSOL simulation of NiFe/Cu/NiFe device and extraction of κ	64

LIST OF FIGURES

6

5.7	Electrical GMR of Co/Cu/Co	66
5.8	Seebeck Voltage at Pt2 of Co/Cu/Co device showing thermal GMR	67
5.9	Results of COMSOL simulation of Co/Cu/Co device and ex- traction of κ	68
6.1	A schematic of the device	72
6.2	Fabrication steps	73
6.3	Measurement configuration	74
6.4	Thermal signal from device 1	75
6.5	Explanation of the interaction of three different effects in de- vice 1	77
6.6	Dependence on probe configuration	79
6.7	Explanation of the signal in configuration B	80

Chapter 1

Introduction

1.1 Introduction and motivation

As electronic devices get smaller and smaller, the importance of heat has become more and more pronounced. Especially in nanoscale structures, heat generated because of Joule heating has become substantially large[1]. Previously, all this heat energy has been thought of as an undesired waste of energy. But recently, several recent advances showed innovative ways to harvest heat energy in nanoscale devices[2, 3, 4]. In this context, two important questions need to be asked. 1. How we can control and manipulate the flow of heat in nanoscale devices? 2. What are the various ways in which heat current can be used, especially in the context of electronic devices such as logic and memory?

Secondly, throughout the history of the computer, information storage almost always had something to do with magnetism. The first generation

computer, which dates back to times before the discovery of the transistor, used large magnetic drums[5] on which bits of information was stored. These later got replaced by ring shaped magnetic cores[6] and as technology progressed[7], we reached the present state of tunnel-junction[8] based magnetic recording[9, 10] which are till-date the most popular as reliable non-volatile memory.

One of the most important breakthroughs in the evolution of computer memories is the discovery of GMR. By late 1980s, it was possible to epitaxially grow high quality ultra-thin films[11] of magnetic materials. While studying the magnetic coupling of ferromagnetic thin films separated by a thin nonmagnetic layer, Albert Fert[12] and Peter Grünberg[13] found independently that the resistance of the multi-layered structure depends on the relative magnetic orientation of the ferromagnetic layers. This simple observation revolutionized how data is stored in computers and led to their joint Nobel prize for Physics in 2007[14].

The popularity of the GMR led to further exploration of the interface between ferromagnetic(FM) and nonmagnetic(NM) materials. We now know that when a current is passed across a FM/NM interface, spin ‘accumulation’ happens at the interface even in the NM layer. That is, there will be a difference in up-spin and down-spin electron populations near the interface. This difference in populations then diffuses inside the ferromagnet, causing a ‘spin current’ in steady state[15, 16]. Because the spins carry spin angular momentum, when the spin current encounters a ferromagnetic layer before

the spin accumulation decays to nearly zero, the spin angular momentum is transferred to the local magnetic moments, causing a torque. This is known as spin-transfer torque. This was experimentally verified by Slonczewski et al[17], and a mathematical formulation was developed[18]. Spin-transfer-torque based fast and non-volatile Magnetic Random Access Memories or STT-MRAMs, which are a very recent invention[19] are based on this concept.

These concepts of GMR, spin current and spin-transfer-torque, along with several other new findings, together constitute the exciting field of spintronics, opening up new possibilities for low energy computing. Putting these two together namely the importance of heat transport and related effects in nanostructures and the new field of spintronics, we have a branch of spintronics called spin-caloritronics[20], where the interaction of electron spin angular momentum, heat and electrical current is studied.

Given that electrical and thermal current in metals are closely related to each other as we will see in detail in chapter 2, the idea is to experimentally verify the thermal analogues of three of the well known spintronic phenomena, which are 1. spin transfer torque, 2. Giant Magnetoresistance (GMR) and 3. Anomalous Hall effect

1.2 Outline of chapters

Chapter 1 gives a short introduction to this research. The importance of heat transport in nanoscale structures and the exciting new nature of the field of spintronics are discussed. Finally, the motivation for this research is shown.

Chapter 2 discusses the theory and background in detail. Starting from spin-independent electron transport, the first part of it shows the relation between thermal and electrical transport and also spin-dependent electron transport. In the second part, relevant spintronic phenomena such as Anisotropic magnetoresistance(AMR), Giant Magnetoresistance(GMR), Ferromagnetic Resonance(FMR), Anomalous Hall effect and spin-transfer-torque are discussed.

Chapter 3 shows the important fabrication and measurement methods involved. Under fabrication, the lithography and deposition processes are discussed in detail. The deposition tools used for this are also described. Under measurement, Scanning Electron Microscopy for imaging, Vector Network Analyzer for measuring dynamics and lock-in measurement system are explained.

Chapter 4, Chapter 5, Chapter 6 are the chapters for three different experiments where thermal analogues are found experimentally for three corresponding spintronic phenomena.

Chapter 4 is about thermally generated spin-transfer-torque. Upon heating a Ferromagnet/Nonmagnet/Ferromagnet trilayer externally using Joule heating, we show evidence for spin transfer torque by looking at the change in the magnetization dynamics.

Chapter 5 is about thermal analogue of giant Magnetoresistance(GMR). By using Pt wires as heating elements and Seebeck effect-based thermometers, we study the flow heat current in-plane in GMR nanowires. We also show that the MR ratio is much higher in case of thermal GMR.

Chapter 6 is about thermal analogue of anomalous Hall effect. By using this anomalous thermal Hall effect, we explain a previously unexplained asymmetry in the thermal spin injection signal in a lateral spin valve in non-local configuration.

Chapter 7 shows a brief summary of the thesis.

Chapter 2

Theory and background

2.1 Introduction

Electrons form the basis of the electrical transport. When it comes to metals, electrons also are the dominant means of thermal transport[21], which is the flow of heat. Thus, to study electrical or thermal transport in metals, we need to understand the behaviour of electrons. The way electrons are arranged into energy levels almost solely determines the transport properties. In this chapter, we will try to understand how this fundamental concept leads to several interesting implications.

2.2 Spin-independent electron transport

In one of the accepted theories of conduction in metals, the conduction electrons, which are from the outermost orbitals, are floating freely in a

periodic potential[22] caused by the lattice. The arrangement of atoms determines the periodic potential, which in turn determines the number of available states at a given energy level. The second big contribution to electron arrangement is the Fermi function f which determines given a certain number of states available, how likely they are to be occupied.

When the electrons fill all the available energy states, there are no neighbouring states available for the electrons to hop into. This shape of the Fermi level has a fundamental implication. That is, well below the Fermi level μ , transport cannot happen. Much above the Fermi level, there are no electrons available in the first place, so transport cannot happen. Therefore, much of the conductivity in the metals comes from electrons with energies near the Fermi level. The number of electrons flowing per unit time(number current) j_n can be quantitatively expressed as

$$j_n = -2e \int d\varepsilon \left(-\frac{\partial f}{\partial \varepsilon} \right) \sigma(\varepsilon) \left(1 - \frac{\varepsilon - \mu}{T} \nabla T \right) \quad (2.1)$$

Where $\sigma(\varepsilon)$ is number conductivity (which is electrical conductivity/electron charge) at the Fermi level.

2.3 Electrical and thermal transport

Since electrons carry electrical charge with them, the electrical current j is simply given by multiplying the number current j_n with electron charge e^- .

$$j = -ej_n = 2e^2 \int d\varepsilon \left(-\frac{\partial f}{\partial \varepsilon} \right) \sigma(\varepsilon) \left(1 - \frac{\varepsilon - \mu}{T} \nabla T \right) \quad (2.2)$$

As for heat current, we can define heat current as the thermal energy carried by electrons. But electrons carry both thermal and chemical energy. Therefore, we can define thermal energy carried per unit time as the difference between total energy carried per unit time and the chemical energy carried per unit time.

$$j_q = j_\varepsilon - \mu j_n \quad (2.3)$$

For a given energy level ε , this becomes

$$j_q^\varepsilon = (\varepsilon - \mu) j_n^\varepsilon. \quad (2.4)$$

Substituting this in the equation 2.1, we have

$$j_q = -2e \int d\varepsilon \left(-\frac{\partial f}{\partial \varepsilon} \right) \sigma(\varepsilon) \left(1 - \frac{\varepsilon - \mu}{T} \nabla T \right) (\varepsilon - \mu) \quad (2.5)$$

Thus, in metals, thermal and electrical transport are closely related. We can combine the two into a matrix equation

$$\begin{pmatrix} j \\ j_q \end{pmatrix} = \begin{pmatrix} L^{11} & L^{12} \\ L^{21} & L^{22} \end{pmatrix} \begin{pmatrix} E' \\ -\nabla T \end{pmatrix} \quad (2.6)$$

where the matrix coefficients are given by[22]

$$L^{11} = \sigma \quad (2.7)$$

$$L^{21} = TL^{12} = -\frac{\pi^2}{3e} (k_B T)^2 \sigma' \quad (2.8)$$

$$L^{22} = \frac{\pi^2}{3} \frac{k_B^2 T}{e^2} \sigma \quad (2.9)$$

$$\sigma' = \frac{\partial \sigma}{\partial \varepsilon} \quad (2.10)$$

The coefficients L_{11} and L_{22} are related by a factor of LT where L is the Lorenz number given by

$$L = \frac{\pi^2}{3} \frac{k_B^2}{e^2} \quad (2.11)$$

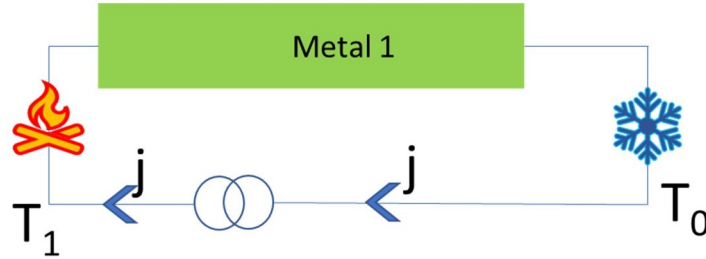


Figure 2.1: Peltier effect

where k_B is the Boltzmann constant. This relation is known as Wiedemann-Franz law. Essentially, this says that at a given temperature, thermal conductivity κ is proportional to the electrical conductivity σ .

2.3.1 Thermo-electric effects

From the above section, we can also see that a thermal gradient ΔT can cause an electrical current and an electrical field E can cause a heat current because both of them arise from the flow of electrons. This class of effects is known as thermoelectricity. The terms L_{12} and L_{21} in the equation 2.6 correspond to the respective thermoelectric effects.

Peltier effect

Let us suppose we apply an electrical current j across a metal. The coefficient L_{21} means that a thermal current j_q is generated. As a result, at the end of the boundaries, heating/cooling can be observed. Mathematically,

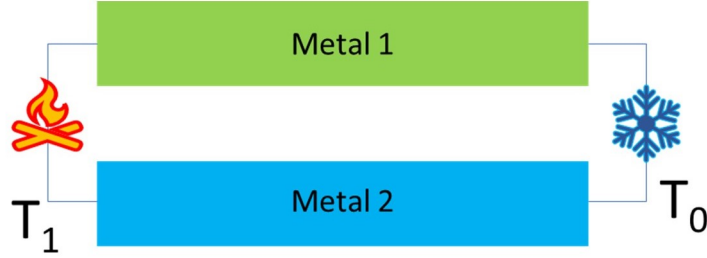


Figure 2.2: Seebeck effect

j_q can be expressed as

$$j_q = \Pi j \quad (2.12)$$

where Π is known as Peltier coefficient, and is given by

$$\Pi = \frac{L_{21}}{L_{11}} \quad (2.13)$$

Seebeck effect

On the other hand, if we apply a thermal gradient ∇T across a metal, it generates a heat current j_q , which in turn generates electric field E across the metal. In an open circuit condition in steady state, this generates a corresponding voltage across the metal, which is known as Seebeck voltage. The generated electric field E is related to the applied thermal gradient ∇T by Seebeck coefficient S .

$$E = S \nabla T \quad (2.14)$$

where S is given by

$$S = \frac{L_{12}}{L_{11}}. \quad (2.15)$$

However, this is open circuit voltage and to measure this voltage, we need some form of electrical contact using a different metal. Therefore, typically, Seebeck voltage is measured as a relative value between two metals. Two metals with different Seebeck coefficients generate a measurable current flow in the loop formed by the two metals. Thus, any two metals with different Seebeck Coefficients are said to form a ‘thermocouple’.

2.4 Spin-dependent electron transport

In the equation 2.1, we used a factor of two that comes from Pauli’s exclusion principle, because both up-spin and down-spin electrons contribute to the current equally. However, if the conductivity of up-spin and down-spin electrons are different, we will have to re-write the expression for electrical current as

$$j^{\uparrow/\downarrow} = e^2 \int d\varepsilon \left(-\frac{\partial f}{\partial \varepsilon} \right) \sigma^{\uparrow/\downarrow}(\varepsilon) \left(1 - \frac{\varepsilon - \mu^{\uparrow/\downarrow}}{T} \nabla T \right). \quad (2.16)$$

We need to note here that if up-spin electrons in one channel can somehow become down-spin electrons through some scattering mechanism, the above expression is not valid. This assumption is called two-current model[23], where the conductivity of the two spin channels is treated separately. Mathematically, this is the same as having two parallel paths for electrical currents. As we will see later, this can qualitatively explain a lot of the spintronic phenomena.

In ferromagnets where the population of up-spin and down-spin electrons are different, this will lead to several interesting observations.

2.4.1 Anisotropic Magnetoresistance

Anisotropic Magnetoresistance (AMR)[24, 25] is a phenomenon where the conductivity of a ferromagnetic material shows anisotropy. That is, the conductivity is dependent on the direction of the flow of electric current with respect to the easy-axis of the ferromagnetic material and the external magnetic field.

2.4.2 GMR

In the years 1988-89, Fert[12] and [13] separately discovered that when thin layers of alternating ferromagnet(FM) and nonmagnetic metal(NM) are grown, the resistance of the whole structure depends on the relative magnetic orientation of the ferromagnets[26]. The simplest version of this would be a trilayer made up of FM/NM/FM. Since the change in resistance is substantially large, this phenomenon is called the Giant Magnetoresistance (GMR) and was used in computer memories[27] until it eventually led to the modern form of tunnel-junction based computer hard-disk drives. GMR is a direct result of spin-dependent conductivity.

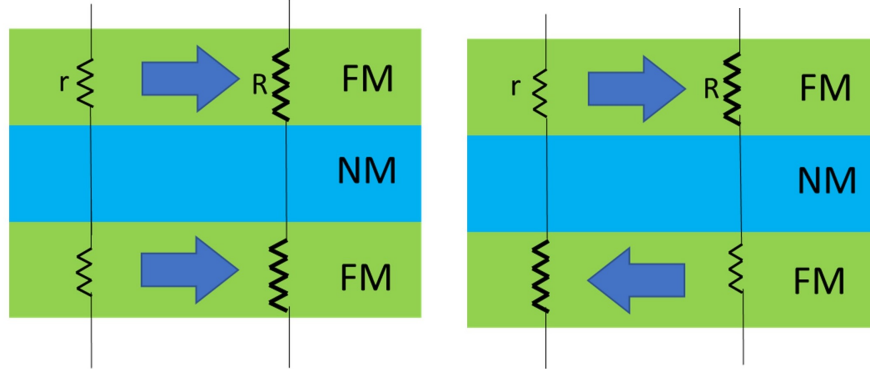


Figure 2.3: GMR in perpendicular-to-plane configuration

current-perpendicular-to-plane

First, we will look at the case when current is flown perpendicular to the FM/NM/FM interfaces. This is known as current-perpendicular-to-plane (CPP) geometry. Figure 2.3 shows an illustration of how GMR works. Let us say r and R are the resistances for majority and minority spin channels respectively[28] and $r \ll R$. When the ferromagnetic layers are oriented parallel to each other, it means that one of the spin channels has resistivity $r + r$ and the other has $R + R$. The effective resistance R_P will be

$$R_P = (r + r) \parallel (R + R) = \frac{2rR}{r + R} \approx 2r. \quad (2.17)$$

In the anti-parallel case, both the spin channels have a resistance of $r + R$. Therefore we have

$$R_{AP} = (r + R) \parallel (r + R) = \frac{r + R}{2} \approx \frac{R}{2}. \quad (2.18)$$

Thus, the parallel and anti-parallel configurations have a large difference in resistance, leading to GMR. The Magnetoresistance(MR) ratio is given by

$$\text{MR} = \frac{R_{AP} - R_P}{R_P} \quad (2.19)$$

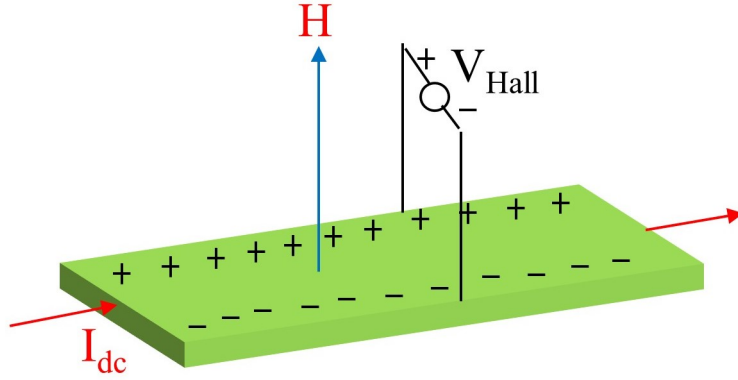


Figure 2.4: Hall effect

2.4.3 Hall effects

Hall effect is the direct result of a Lorentz force caused by a magnetic field on current carrying electrons in a conductor. When magnetic field is applied onto a current carrying conductor, the electrons are pushed in a direction perpendicular to the applied magnetic field and the current flow. Since the Lorentz force by a magnetic field \mathcal{B} on an electron moving at a velocity \mathbf{v} is given by

$$\mathcal{F}_{\text{Magnetic}} = -e\mathbf{v} \times \mathcal{B}, \quad (2.20)$$

the electrons are pushed in a direction same as that of $v \times B$. However, since electrons cannot flow continuously in the transverse direction, in steady state, this results in a measurable voltage perpendicular to the original current and the applied field. We can define the Hall coefficient R_H as

$$R_H = \frac{V_H t}{IB} \quad (2.21)$$

where I is the current flowing, V_H is the measured Hall voltage and t is the thickness. The discovery of Hall effect[29] in 1879 in normal metals is a

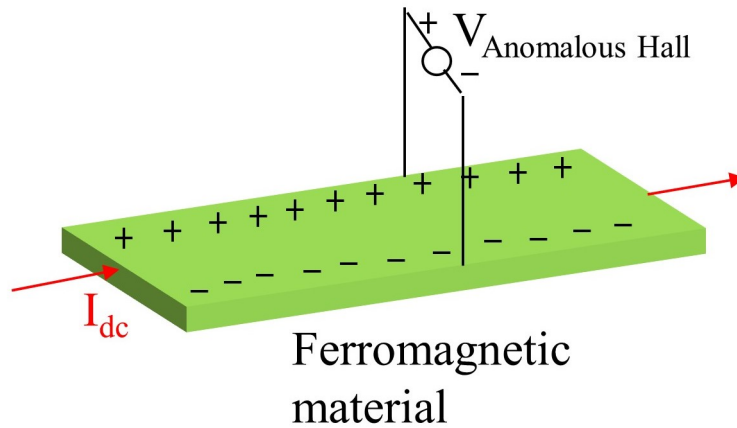


Figure 2.5: Anomalous Hall effect

starting point for the subsequent several effects of similar fundamental origin in ferromagnetic metals. Hall effect can be used to make an efficient and inexpensive magnetic field sensor.

Anomalous Hall effect

Anomalous Hall effect is similar to Hall effect, but can be found in the absence of a magnetic field. When a current is flown through a ferromagnetic material, it is known that a Hall Voltage can be observed in the absence of external magnetic field[30]. However, the magnitude of this voltage is unusually large and the internal magnetic fields alone cannot account for this quantitatively. Nagaosa et al[31] have reviewed the phenomenon and identified three different causes. They are

1. Intrinsic deflection - arising from ‘Berry phase’[32]. The electrons flowing in a ferromagnetic material with nonzero Berry phase, intrinsically

have a velocity perpendicular to the applied electric field. This is known as ‘anomalous velocity’[33].

2. Spin dependent scattering - When the electron approaches an impurity, it experiences a scattering electric field which is dependent on spin. The two spins may be deflected in the opposite directions, which cause a transverse voltage. The asymmetric scattering can also be due to spin-orbit coupling.

2.5 Magnetization dynamics

Let us define a local magnetic moment as the vector \mathcal{M} . The force experienced by the magnetic moment in an external magnetic field \mathcal{H}_{ext} influences it as

$$\frac{d\mathcal{M}}{dt} = \mu_0\gamma\mathcal{M} \times \mathcal{H}_{eff} \quad (2.22)$$

where \mathcal{H}_{eff} is the effective magnetic field after accounting for the demagnetizing field, γ is the gyromagnetic ratio given by

$$\gamma = \frac{ge}{2mc} \quad (2.23)$$

where g is the Lande g -factor, e is the charge of an electron, m is the mass of electron and c is the speed of light in vacuum. Since $\frac{d\mathcal{M}}{dt}$ is perpendicular to \mathcal{M} , it causes the \mathcal{M} to precess around the magnetic field. However, similar to friction when mechanical motion is involved, there is a damping here which needs to be accounted for. After adding the damping factor, we arrive at the famous Landau-Lifshitz-Gilbert(LLG) equation.

$$\frac{d\mathcal{M}}{dt} = \mu_0\gamma(\mathcal{M} \times \mathcal{H}_{eff}) - \frac{\alpha}{M_s} \left(\mathcal{M} \times \frac{d\mathcal{M}}{dt} \right) \quad (2.24)$$

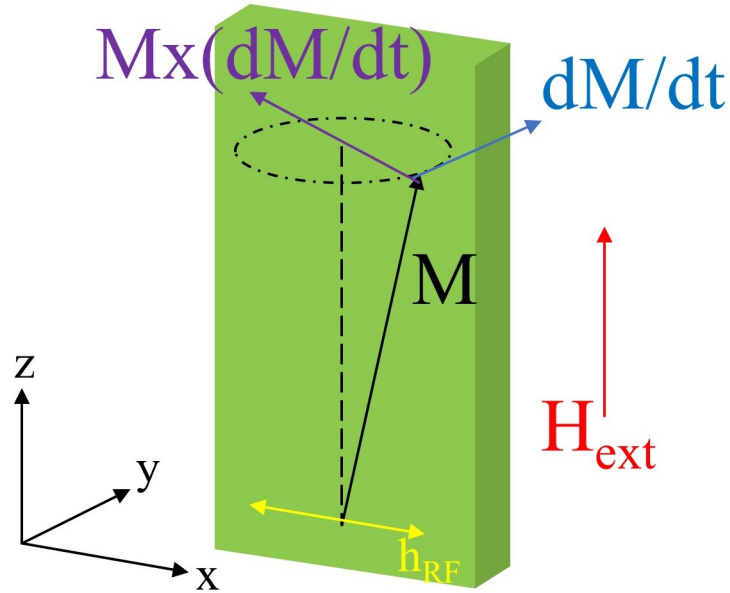


Figure 2.6: Magnetization dynamics under external magnetic field

where M_S is the saturation magnetic field and α is the Gilbert damping factor. This form of LLG equation means that while the external magnetic field tends to cause precession around that magnetic field, the damping term causes the precession to dampen and disappear.

2.5.1 Ferromagnetic resonance

When we can somehow provide the local moments with an energy using a small oscillating magnetic field at radio frequency (RF) that can balance out the damping, the precession can happen indefinitely. This indefinite precession is the largest when the frequency of applied RF field matches the natural frequency of precession. This phenomenon is called the ferromag-

netic resonance(FMR)[34, 35]. To get a quantitative understanding, let us say a constant field $\mathcal{H}_{\text{ext}} = (0, 0, h_0)$ is applied along the easy axis of a ferromagnetic cuboid of dimensions $l \times w \times t$ where $l \gg w \gg t$ as shown in figure 2.6. Let the applied RF magnetic field be h_{RF} along the x-axis. The effective field will be given by

$$\mu_0 \mathcal{H}_{\text{eff}} = (\mu_0 h_{\text{RF}} - N_x m_x, -N_y m_y, \mu_0 h_0) \quad (2.25)$$

where N_x, N_y are the demagnetization factors where

$$N_x + N_y = 1 \quad (2.26)$$

and the local magnetic moment \mathcal{M} is given by

$$\mathcal{M} = (m_x, m_y, M_s). \quad (2.27)$$

Substituting these in the LLG equation 2.24, we get

$$\begin{pmatrix} \frac{\partial}{\partial t} & -\gamma(\mu_0 h_0 + N_y M_s) - \alpha \frac{\partial}{\partial t} \\ \gamma(\mu_0 h_0 + N_x M_s) + \alpha \frac{\partial}{\partial t} & \frac{\partial}{\partial t} \end{pmatrix} \begin{pmatrix} m_x \\ m_y \end{pmatrix} = -\gamma M_s \begin{pmatrix} 0 \\ \mu_0 h_{\text{RF}} \end{pmatrix}. \quad (2.28)$$

Upon Fourier transform, this becomes

$$\begin{pmatrix} -i\omega & \gamma(\mu_0 h_0 + N_y M_s) + i\omega\alpha \\ \gamma(\mu_0 h_0 + N_x M_s) - i\omega\alpha & -i\omega \end{pmatrix} \begin{pmatrix} m_x \\ m_y \end{pmatrix} = -\gamma M_s \begin{pmatrix} 0 \\ \mu_0 h_{\text{RF}} \end{pmatrix} \quad (2.29)$$

Finally, we derive the complex susceptibility tensor as

$$m_x = \chi h_{\text{RF}} \quad (2.30)$$

where

$$\chi = \chi' + i\chi'' \quad (2.31)$$

$$\chi' = \frac{\omega_x \omega_M (\omega_0^2 - \omega^2)}{(\omega_0^2 - \omega^2)^2 + \alpha^2 \omega^2 (\omega_x + \omega_y)^2} \quad (2.32)$$

$$\chi'' = \frac{\alpha \omega \omega_M (\omega_y^2 - \omega^2)}{(\omega_0^2 - \omega^2)^2 + \alpha^2 \omega^2 (\omega_x + \omega_y)^2} \quad (2.33)$$

$$\omega_0^2 = \gamma^2 (\mu_0 h_0 + N_x M_s) (\mu_0 h_0 + N_y M_s) \quad (2.34)$$

$$\omega_x = \gamma (\mu_0 h_0 + N_x M_s) \quad (2.35)$$

$$\omega_y = \gamma (\mu_0 h_0 + N_y M_s) \quad (2.36)$$

$$\omega_M = \gamma (M_s) \quad (2.37)$$

The χ' and χ'' follow an anti-Lorentzian and Lorentzian shape respectively when plotted against the RF frequency ω . Since the imaginary part in the Fourier transform is proportional to the energy absorption, the S-parameter measured in chapter 3 will show a Lorentzian shape.

2.5.2 Spin-transfer torque

When spin current is passed into a ferromagnet, the spin angular momentum carried by the spin current gets transferred to the local moments and causes a torque. This is known as spin transfer torque[17, 36]. This spin transfer torque alters the dynamics defined by the LLG equation. Zhang, Levy and Fert[18] derived a mathematical expression for the influence of spin transfer torque on magnetization dynamics. However, we are modifying

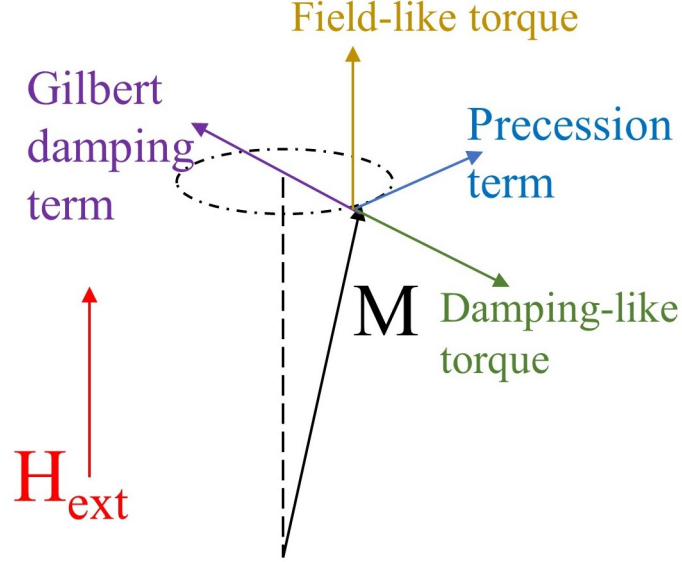


Figure 2.7: Magnetization dynamics under spin transfer torque

it slightly by considering N_x and N_y instead of ignoring the demagnetizing field along two of the axes. During the experiment in chapter 4, we found that N_x is low but not negligible. Zhang et al started by defining an interaction Hamiltonian

$$H_{\text{interaction}} = -J\mathbf{m} \cdot \mathcal{M} \quad (2.38)$$

Where \mathbf{m} is the incoming magnetic moment. This is mathematically very similar to the energy of a magnetic moment in an external magnetic field.

$$H_{\text{local}} = -\mu_0\mathcal{H}_{\text{eff}} \cdot \mathcal{M} \quad (2.39)$$

Therefore, we assume that the LLG equation is modified as if $J\mathbf{m}$ acts similar to applied magnetic field. Now, the modified LLG equation will be

$$\frac{d\mathcal{M}}{dt} = \mu_0\gamma(\mathcal{M} \times (\mathcal{H}_{\text{eff}} + Jm)) - \frac{\alpha}{M_s} \left(\mathcal{M} \times \frac{d\mathcal{M}}{dt} \right) \quad (2.40)$$

Since the perpendicular moment decays much faster than the parallel moment, it is the major contributor to the spin transfer torque. Therefore,

$$\frac{d\mathcal{M}}{dt} = \mu_0\gamma (\mathcal{M} \times (\mathcal{H}_{\text{eff}} + J\mathbf{m}_{\perp}\mathcal{M})) - \frac{\alpha}{M_s} \left(\mathcal{M} \times \frac{d\mathcal{M}}{dt} \right). \quad (2.41)$$

Let us say $\mathbf{m} = (0, m \sin \theta, m \cos \theta)$ where θ is the angle between injected magnetic moments and local ones

$$\mathbf{m}_{\perp} = (0, m \sin \theta, 0) \quad (2.42)$$

$$\mathcal{M} = (\sin \phi, 0, \cos \phi), \quad (2.43)$$

where ϕ is the precession cone angle

\mathbf{m}_{\perp} can be resolved along $\mathcal{M}, \mathcal{M} \times \mathbf{m}, \mathcal{M} \times (\mathcal{M} \times \mathbf{m})$.

$$\frac{d\mathcal{M}}{dt} = \gamma (\mathcal{M} \times (\mu_0\mathcal{H}_{\text{eff}} + Jm^2 \sin^2 \theta)) - \frac{\alpha}{M_s} \left(\mathcal{M} \times \frac{d\mathcal{M}}{dt} \right) + Jm^2 \sin \theta \cos \theta \sin \phi \quad (2.44)$$

will be the final form of modified LLG. However, since the value of J is not theoretically derived, we replace the terms with a and b representing damping-like and field-like torque, respectively.

$$\frac{d\mathcal{M}}{dt} = \gamma (\mathcal{M} \times (\mu_0\mathcal{H}_{\text{eff}} + b)) - \frac{\alpha}{M_s} \left(\mathcal{M} \times \frac{d\mathcal{M}}{dt} \right) + a\mathcal{M} \times (\mathcal{M} \times \mathbf{m}). \quad (2.45)$$

We need to note that although it seems like spin transfer torque is zero when the angle θ is zero, a small initial disturbance can cause precession, which increases the θ and creates a positive feedback loop. Thus, it is possible to generate spin transfer torque although the injected spins are not at an angle to the local magnetic moment.

Chapter 3

Fabrication and measurement methods

All the experiments discussed in this thesis involve fabrication of thin films of the order of a few nanometers and sub-micron patterning down to the level of a 100nm. Therefore, it is important to understand the fabrication process well to repeat the experiments reliably. Therefore, this chapter will show the details of fabrications steps. Additionally this chapter also presents the measurement methods involved which are Vector-Network-Analyzer(VNA) based Ferromagnetic Resonance (FMR), lock-in measurement technique for filtering the first of second harmonic of the output signal.

3.1 Fabrication steps

3.1.1 Lithography

Most of the patterns were made using electron-beam lithography followed by lift-off, except when a hard metal mask was used. Electron-beam lithography (usually referred to as EBL) this takes advantage of the fact that the DeBroglie wavelength of electrons is much smaller than that of the ultra-violet light which is used for conventional optical lithography process. First, we spin-coat a chemical known as e-beam resist (as opposed to photoresist in optical lithography) which in our case is ZEP on the substrate and then bake it at 180°C for solidifying.

Then, we subject it to electron-beam radiation only in the areas where a pattern is to be made. The exposure to the electron radiation makes the resist soft in the exposed area by changing its chemical property. Then, the sample is washed in O-Xylene, which reacts only with the softened part of the resist. This leaves the exposed area empty, surrounded by resist in the unexposed area. Please note that the thickness of the resist should be at least 10 times larger than the thickness of the thin film pattern to be made. In our case, it was either $1\mu\text{m}$ or $3\mu\text{m}$ corresponding to a spin-coating speed of 5000rpm or 3000rpm respectively. Finally, we deposit the material on top of the pattern and then strip the resist using a remover which in our case is N,N Dimethyl Acetylamide (also known as Z-Dimethyl Acetylamide or ZD-MAC). This stripping process only leaves the pattern on the sample where it is desired. This is commonly known as lift-off.

Exposure process

The instrument used was Elionix-7800, which allows an acceleration voltage of 80kV and has a laser to accurately adjust the stage height. The pattern is made into a CAD file which is read by a computer. The e-beam which is accelerated to a high voltage is focused into a very narrow beam with diameter of about 2nm, and is controlled by the computer. The substrate is then exposed according to the pattern defined by the CAD file. The parameters that we need to take care of during the exposure process are

1. dosage - amount of electrons hitting unit area of the sample - the property of the resist determines how much dose is to be used, but subtle adjustments should be made according to the substrate and the pattern
2. chip size - the area of sample which is considered as a single unit and is exposed at a time - larger chip sizes can be used for larger patterns so that there is no breaking.
3. dot size - the machine treats the pattern as an aggregation of very tiny dots which are like pixels in an image - the finer the resolution, the sharper the pattern is.

3.1.2 Deposition

For deposition of metals, we used sputtering, e-beam evaporation or Joule evaporation techniques. Sputtering is the process of hitting the source with high energy Ar ions and making the source molecules jump off the surface.

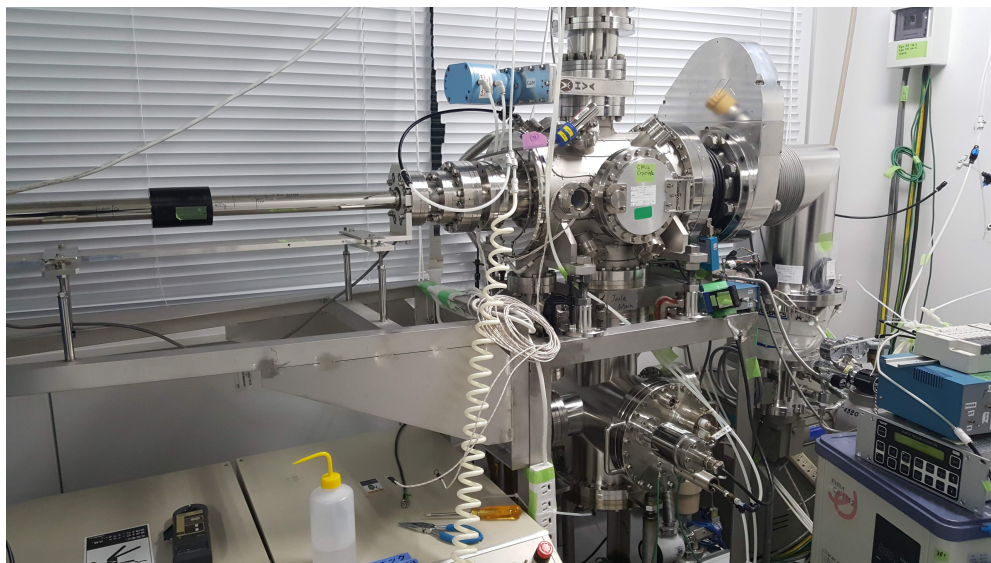


Figure 3.1: Joule evaporation/triple source e-beam evaporation setup

Since this is performed at high-vacuum, the mean free path of the molecules is very large, and hence travel directly to the substrate and get deposited. Joule evaporation and e-beam evaporation are the techniques where the source is melted and evaporated by using Joule heating upon passing a very high current, or by hitting the source with an electron-beam. Again, it is done in a high vacuum to give the molecules a large mean free path.

Three machines were used for this purpose.

Joule evaporation + 3-source e-beam evaporation system

The essence of this system is to let us deposit the Ferromagnet/Nonmagnet heterostructures without breaking the vacuum. It also has a low-power ion-milling system inside it. It is powered by a cryo-pump and a turbo-mechanical



Figure 3.2: DC/RF Sputter machine with several sources out of which we used Pt and W for the following experiments

pump and can generate an ultra high vacuum of upto 1×10^{-7} Pa. On the ferromagnet side, we can choose between CoFeAl, Co or NiFe as the sources, and Cu is deposited using the Joule evaporation system. As shown in figure 3.1, a magnet based sample moving system allows us to move the sample between Cu and ferromagnet deposition areas without opening the door, thus maintaining the vacuum. There is a thickness monitor installed inside to measure the thickness of the deposited material with a precision of 1\AA .

Multi-Sputtering system

This machine has several DC and RF sputtering sources, and has a load-lock mechanism for achieving the vacuum very quickly. Out of these several sources, we used only Pt and W in the following experiments, whose depo-

sition rates are pre-calculated at given deposition conditions. Both of these metals use a DC sputtering power of 60W and we use a load-matching unit to ensure that reflected power is kept to the minimum. Figure 3.2 shows a picture of this system.

Mini-sputtering system

This machine is used to deposit SiO_2 using RF sputtering mechanism. The working mechanism is very similar to the above described multi-sputter system. It is important to note that to deposit insulators such as SiO_2 , we need to use RF because DC would cause a charge build-up and can create sparks and shorting.

3.2 Measurement methods

3.2.1 Vector Network Analyzer - Ferromagnetic Resonance

Vector Network Analyzer (VNA) is a tool that sends a low-power RF excitation across a 50Ω load, and measures the S-parameter as a function of the frequency. It can work from 300MHz to 20GHz and operates with a very low noise. This allows a sensitive measurement of Ferromagnetic Resonance (FMR). In our experiment, we fabricated a coplanar waveguide (CPW) made of Cu separated by SiO_2 on top of the device, and connected the VNA port

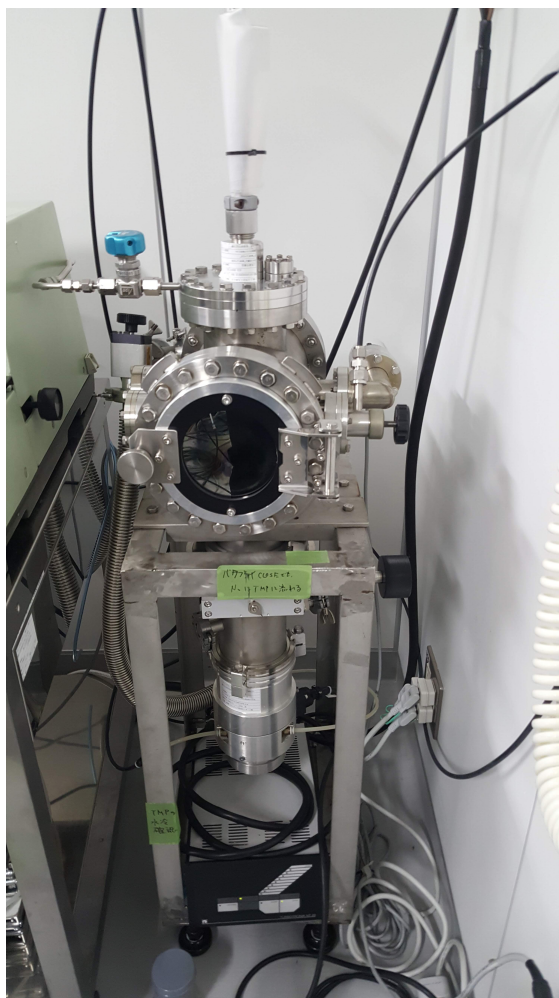


Figure 3.3: RF Sputter machine for SiO₂

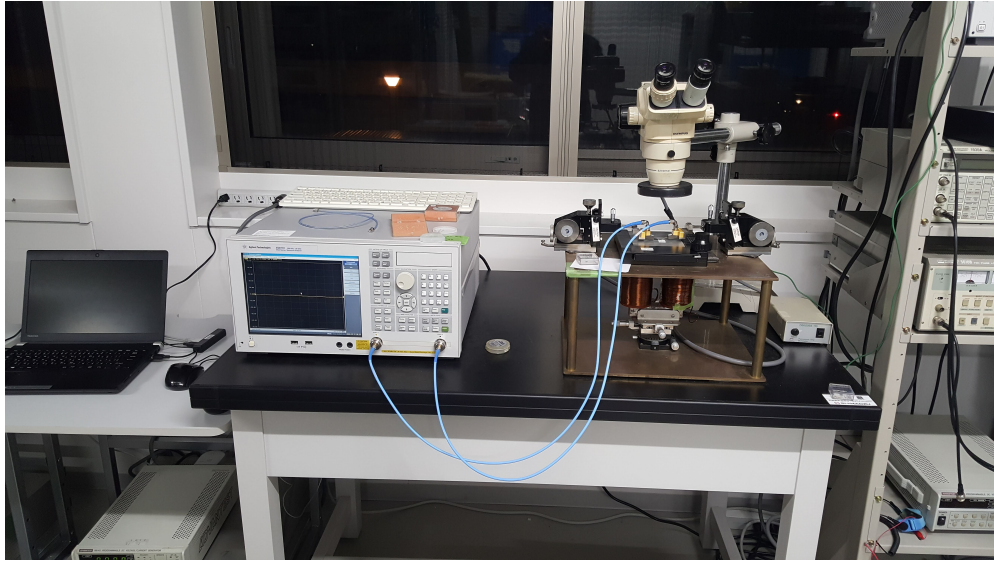


Figure 3.4: Vector Network Analyzer setup

to the CPW. When a part of the device is undergoing FMR, as shown in the chapter 2, the S-parameter changes, thus causing a distinct Lorentzian peak in the frequency response of the VNA. This can be identified as the FMR and the linewidth and peak position can be accurately measured to understand the magnetization dynamics of the device.

However, when the impedance of the CPW is not perfectly 50Ω , then the frequency response of the VNA contains large additional background signal. In order to remove this, we first measure the background signal at a given magnetic field, and then divide any signal with the background to remove it. Please note that we divide instead of subtract because the frequency response is measured in log scale. Figure 3.4 shows a picture of the VNA-FMR setup.



Figure 3.5: Lock-in measurement setup

3.2.2 Field-dependent lock-in measurement

This setup was used to measure electrical and thermal spin injection signals as well as thermal transport measurements. A picture of the setup is shown in figure 3.5. This setup has two closely spaced large electromagnets which are precisely controlled and calibrated to generate a desired magnetic field in between them. The device, which can have a maximum of 20 electrical connections is placed between the two electromagnets. Any current to be passed or voltage to be measured can be done using these electrical connections. Please note that in order to use this, we need to place the device in a pre-designed chip and wire-bond the contact pads on the chip to the desired places on the device.

An AC current of a very low frequency f_{in} (173Hz in all the following experiments) is applied as an input I_{in} and the output voltage is pre-amplified by a low-noise amplifier with a gain of 1000 and then passed onto a band-pass filter which filters out only the desired frequency which is either the same frequency as I_{in} for first harmonic measurement or double the input frequency for second harmonic measurement. A lock-in amplifier then finds the in-phase and out-of-phase components with respect to the input current with a very high sensitivity. This is called lock-in measurement technique.

Chapter 4

Experiment 1: Thermally driven spin transfer torque

4.1 Introduction

Spin current is the flow of spin angular momentum, which is said to act as an alternative for charge currents[37]. Since spin current carries spin angular momentum, this can be transferred to the local magnetic moments of a ferromagnetic material, causing what is known as spin-transfer-torque. Slonczewski first proposed[17] in 1995 that spin transfer torque could be used for current-driven precession and switching phenomena in magnetic multilayers. Berger[38] expanded this theory and predicted the modification of spin dynamics, especially the Gilbert damping parameter. Tsoi et al[39] showed experimentally the effect of spin-transfer torque on magnetization dynamics, making the predictions of Berger[38] come true. There are several ways in which spin-transfer torque can be detected or put to practical use. The most

important use is switching of the magnetization of a ferromagnet. Myers et al[40], Kimura et al[41] and Sun[42] showed that it is possible to achieve magnetization switching by using spin transfer torque. There are also other unexpected effects arising from spin transfer torque such as the Spin torque diode effect[43]. Several attempts were made to understand the exact nature of the spin transfer torque[44, 45, 46], and its influence on the dynamics[18]. More exciting applications using spin transfer torque were also proposed[47].

On the other hand, thermally driven spin injection has been observed experimentally using several methods. Slachter et al[48] first showed a thermal spin injection into a nonmagnetic material from a ferromagnetic material. Recently, we have seen that a new material CoFeAl can be used to efficiently generate thermal spin injection because of a special property of having opposite signs of Seebeck coefficients for different spins[49, 50]. Combining the above two concepts of thermal spin injection and spin transfer torque, Hatami et al[51] predicted that magnetization switching can be achieved from thermally generated spin transfer torque. So far, Choi et al[52] have shown thermal spin transfer torque using ultrafast heat current generated by picosecond laser pulses. Bose et al[53] showed a change in the switching field, possibly caused by thermal spin transfer torque. Petit et al[54] have found a clear thermal signature in their analysis of the influence of electrical version of spin transfer torque on the magnetization dynamics, but did not take into account the possibility of thermally driven spin transfer torque. Thus, a direct study of the influence of thermally driven spin transfer torque on the magnetization dynamics is in order. Therefore, taking advantage of

the CoFeAl developed in-house, we measured the influence of spin transfer torque generated by thermally injected spin current on the dynamics of NiFe nanodots.

4.2 Sample structure

Figure 4.1 shows a schematic of the device. The central part of the device is the NiFe/Cu/CoFeAl trilayer, with thicknesses 20nm/15nm/10nm respectively. Figure 4.1 shows the side view of the device. The top NiFe layer is etched into numerous small dots of sizes ranging from $200\text{nm} \times 400\text{nm}$ to $1 \mu\text{m} \times 2\mu\text{m}$, to improve spin injection efficiency. On top of the trilayer, there is a Co-planar Waveguide (CPW) made of 200nm thick Cu, separated by 100nm thick SiO_2 . The width and length of this CPW is chosen so that it covers the entire area of the trilayer. At the bottom, there is a W heating element, which is 20nm thick, to provide a resistance which is high enough for generating substantial thermal gradient from Joule heating.

Figure 4.3 shows the fabrication steps. The composition of NiFe is Ni:Fe in the ratio 80:20 as purchased. Since the CoFeAl source was made in-house, the composition of CoFeAl was measured using EDX and verified as Co:Fe:Al in the ratio 48:48:4.

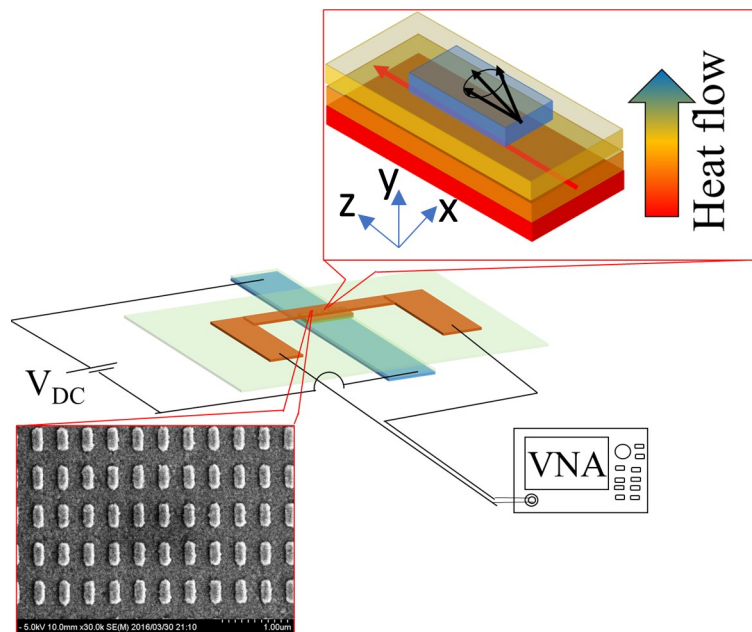


Figure 4.1: A schematic of the device

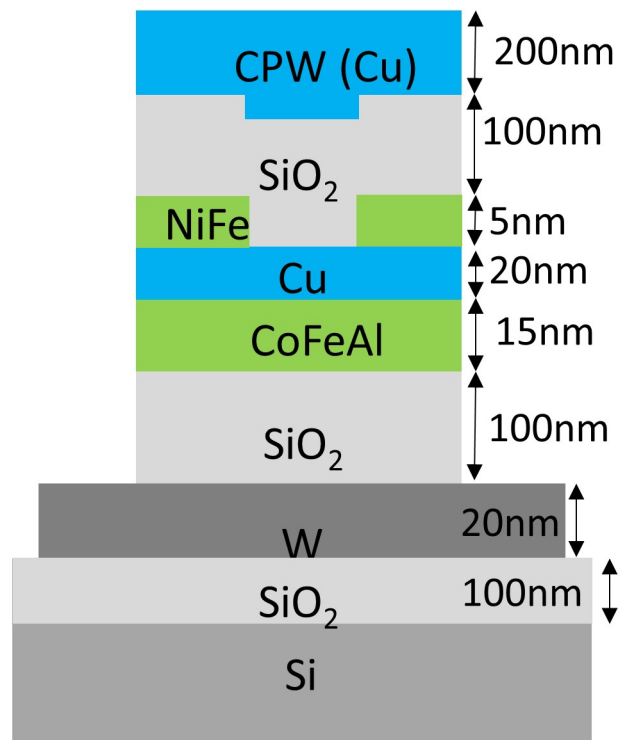


Figure 4.2: Side view of the layers and their thickness

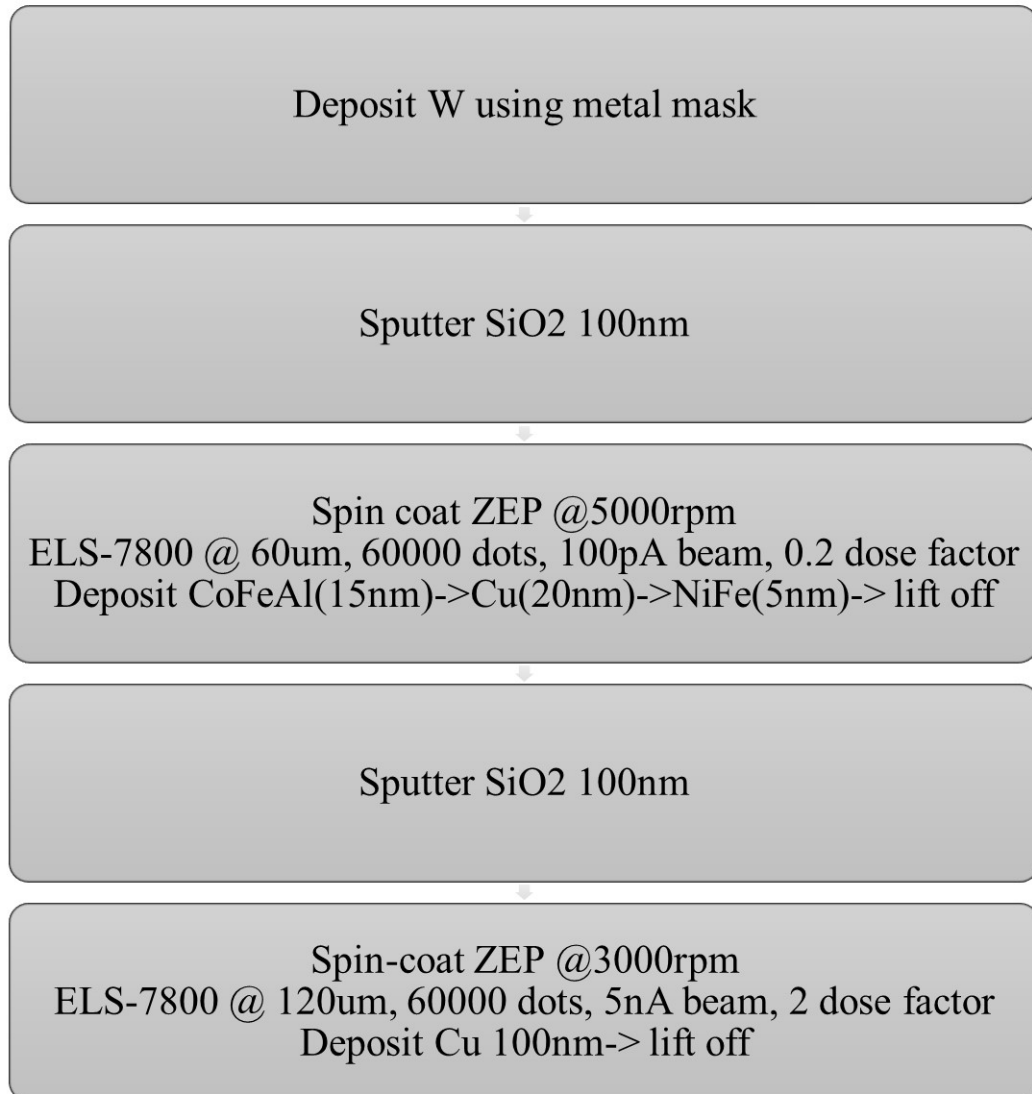


Figure 4.3: Fabrications steps

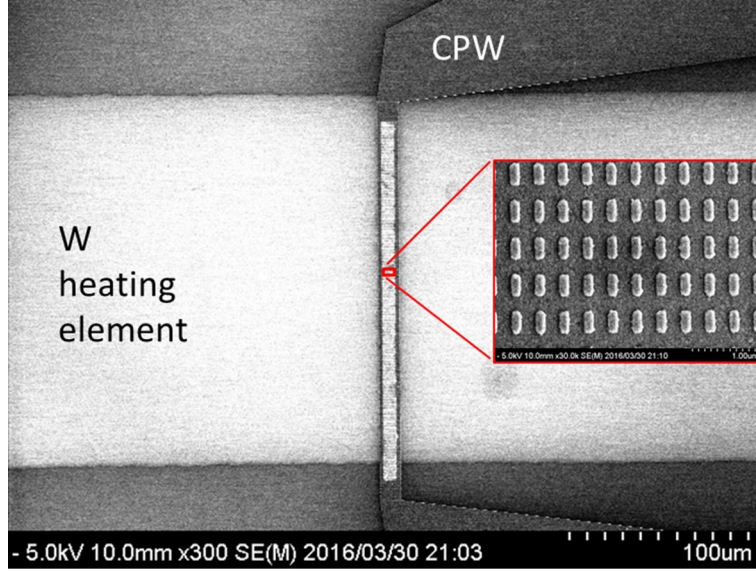


Figure 4.4: SEM image of the the device

4.3 Experiment details

As shown in figure 4.1, the measurement involves connecting a Vector Network Analyzer (VNA) to the CPW and measuring the single port RF scattering parameter S_{11} across a range of frequencies from 300MHz to 16GHz as the output signal of the VNA. Similarly, we measured the signal at different values of applied magnetic field, which was swept from -150mT to 150mT. Since the impedance of the CPW is not perfectly matched with the output impedance of the VNA, there will always be an impedance mismatch component in the frequency response. To eliminate it, we always first measured the frequency response at a given field - say 200mT, which we call the background signal S_{11}^{bg} and divide the signal S_{11} at every field by the background signal S_{11}^{bg} . Please note that here we divided, not subtracted because

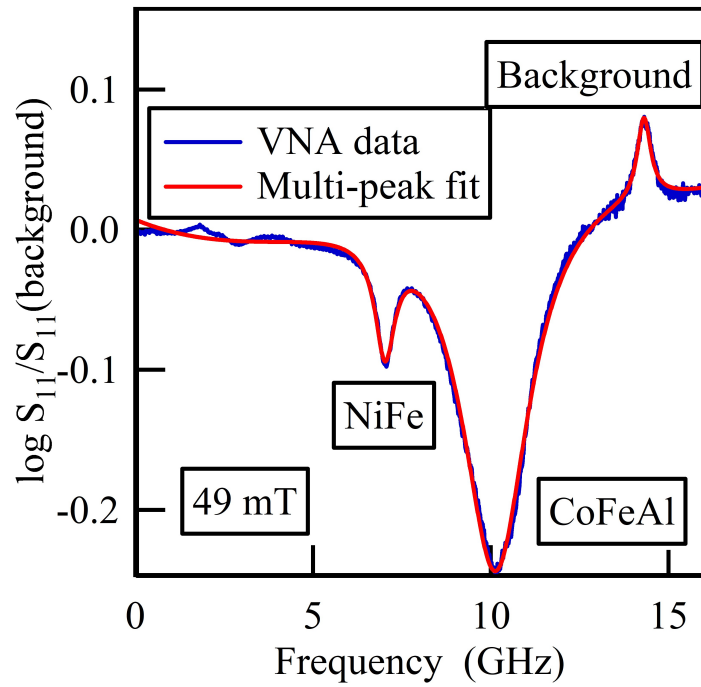


Figure 4.5: Typical signal measured by VNA and corresponding multi-peak fitting

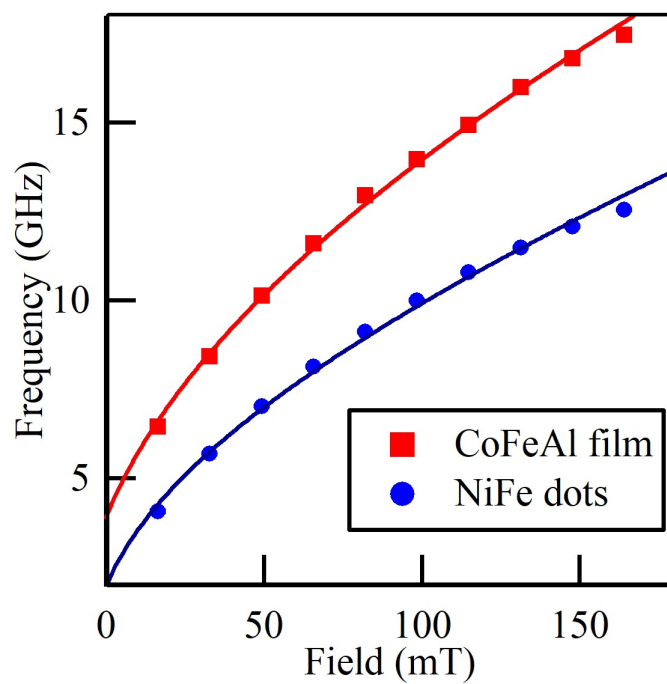


Figure 4.6: Typical signal measured by VNA and corresponding multi-peak fitting

the frequency response is measured in log scale.

To measure the effect of heating, we flowed a DC current varying from 0mA to 200mA through the W heating element, thus generating a vertical temperature gradient across the trilayer. We repeated the above process of getting the frequency response at different values of applied magnetic field for each value of the current.

4.4 Results and Discussion

Firstly, we confirmed by COMSOL simulation by ensuring that there is sufficient temperature gradient across the device. As we can see in figure 4.7, the temperature gradient across the device CoFeAl/Cu/NiFe trilayer alone is 1.5mK across the 40nm thickness, which translates to a gradient of 37500K/m. When an RF current is passed through the CPW, it creates an RF electromagnetic Oersted field around it. And when the frequency matches the natural resonance frequency of the ferromagnet underneath, it causes ferromagnetic resonance (FMR). Since the energy for the FMR comes from the RF magnetic field generated by the CPW, and the S parameters of an RF circuit are inversely related to energy loss, the FMR is seen as an absorption peak in the FMR signal. Chapter 2 shows how this FMR signal is a Lorentzian peak. Figure 4.5 shows a typical S_{11} signal at a given magnetic field (in this case 19mT). We can see two Lorentzian peaks, one each

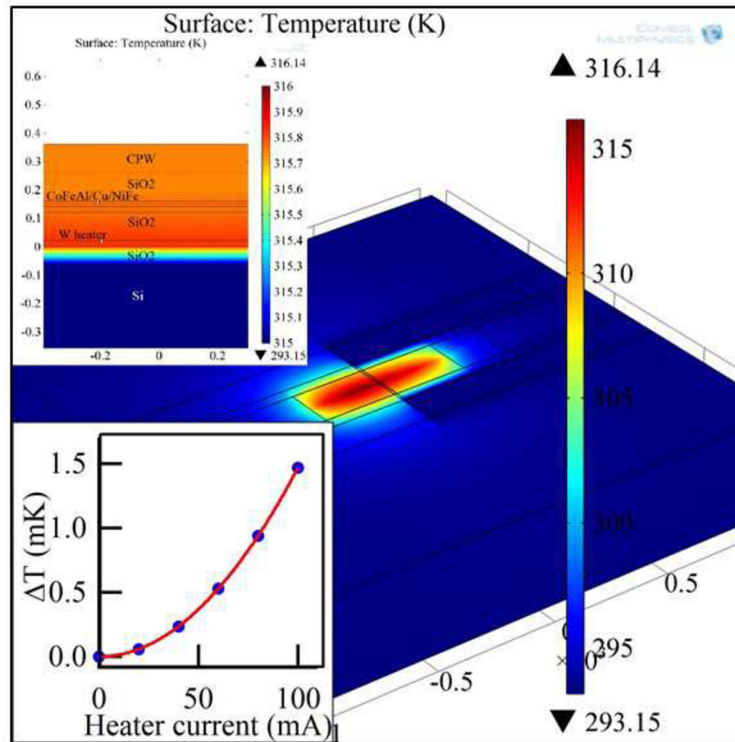


Figure 4.7: Comsol simulation showing the temperature gradient across CoFeAl/Cu/NiFe trilayer in the inset

for CoFeAl and NiFe respectively. The little peak on the right side can be concluded as the background, because the peak position did not vary with the applied field.

The red line in figure 4.5 is a fitting of Lorentzian peaks using the multi-peak fitting function with background in the Igor Pro software. Figure 4.6 shows the positions of those peaks, showing a trend that is expected from the Kittel frequency

$$\omega^2 = \gamma^2 (\mu_0 H_{\text{ext}} + N_x M_s) (\mu_0 H_{\text{ext}} + N_y M_s) \quad (4.1)$$

where γ is gyro-magnetic ratio, H is the applied magnetic field, M_s is the saturation magnetization, N_x and N_y are anisotropy factors, under the constraint $N_x + N_y = 1$. The directions of the axes x, y, z is defined as in figure 4.1. By fitting the Kittel equation to the graph of peak positions vs. applied field, we can estimate that the values of N_x, N_y, M_s are 0.023, 0.977, 0.97T for smaller peak and 0.006, 0.994, 1.58T for larger peak, respectively. Based on this, we can conclude that the smaller peak shown by red dots is from NiFe and that the larger peak shown by blue squares is from CoFeAl. This is consistent with the fact that the total energy absorbed by NiFe dots will be smaller because the total volume is smaller. We can take the error bars as 1σ confidence intervals of the peak fitting, which are not shown because they are smaller than the marker size.

Now, we passed a DC current through the W heating element and made the same measurement. Figure 4.8 shows how the FMR signal at a given applied field (33mT) varied with the DC current. We can see that the position of the CoFeAl peak is not changing as much, but the position of the NiFe

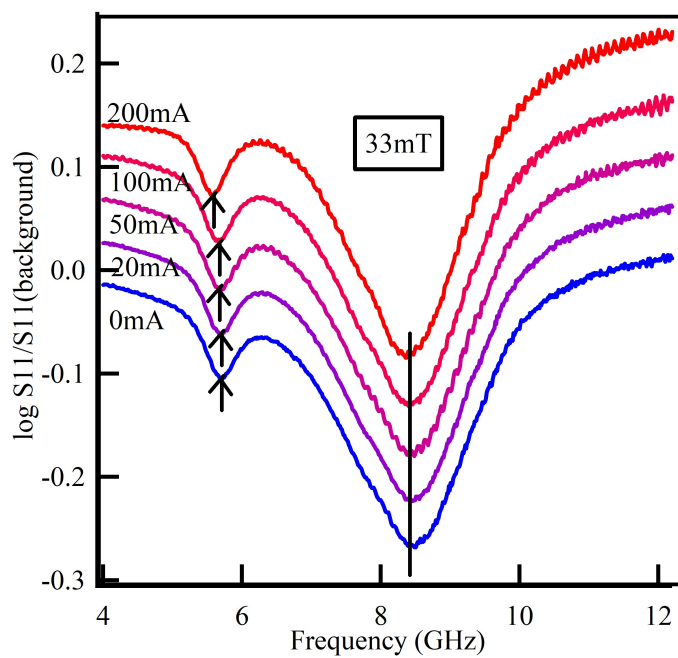


Figure 4.8: Heater current vs VNA signal

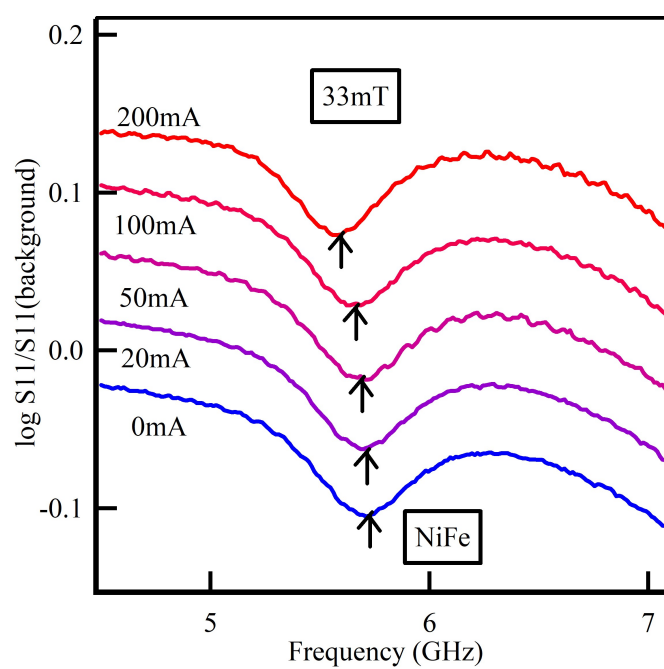


Figure 4.9: Heater current vs VNA signal zoomed in to NiFe peak

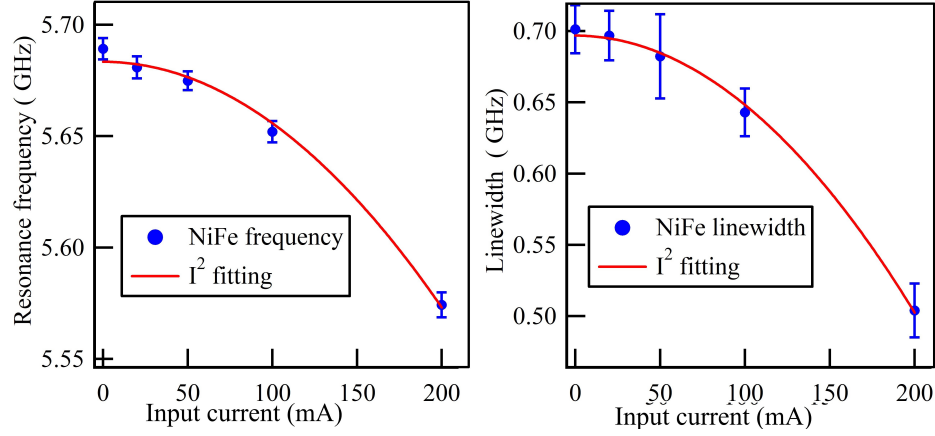


Figure 4.10: Parabolic fit of change in linewidth and frequency vs heater current

peak is shifting towards left as the heating current is increased. Figure 4.9 is a zoomed in version of figure 4.8, showing the left shift more clearly.

We plotted the the FMR frequency as a function of the heater current in figure 4.10, which shows a parabolic trend, owing to the fact that Joule heating is proportional to the I^2 where I is the current. We also plotted the FMR linewidth vs. the heater current, which shows a similar parabolic trend. Again, the error bars in both the above graphs are the 1σ confidence intervals of the peak fitting.

According to Zhang, Levy and Fert[18], as discussed in chapter 2, the modified LLG equation is given by

$$\frac{d\mathcal{M}}{dt} = \gamma (\mathcal{M} \times (\mathcal{H}_{\text{ext}} + b)) - \frac{\alpha}{M_s} \left(\mathcal{M} \times \frac{d\mathcal{M}}{dt} \right) + a\mathcal{M} \times (\mathcal{M} \times \mathbf{m}), \quad (4.2)$$

which means that the FMR will be modified as a change in both FMR fre-

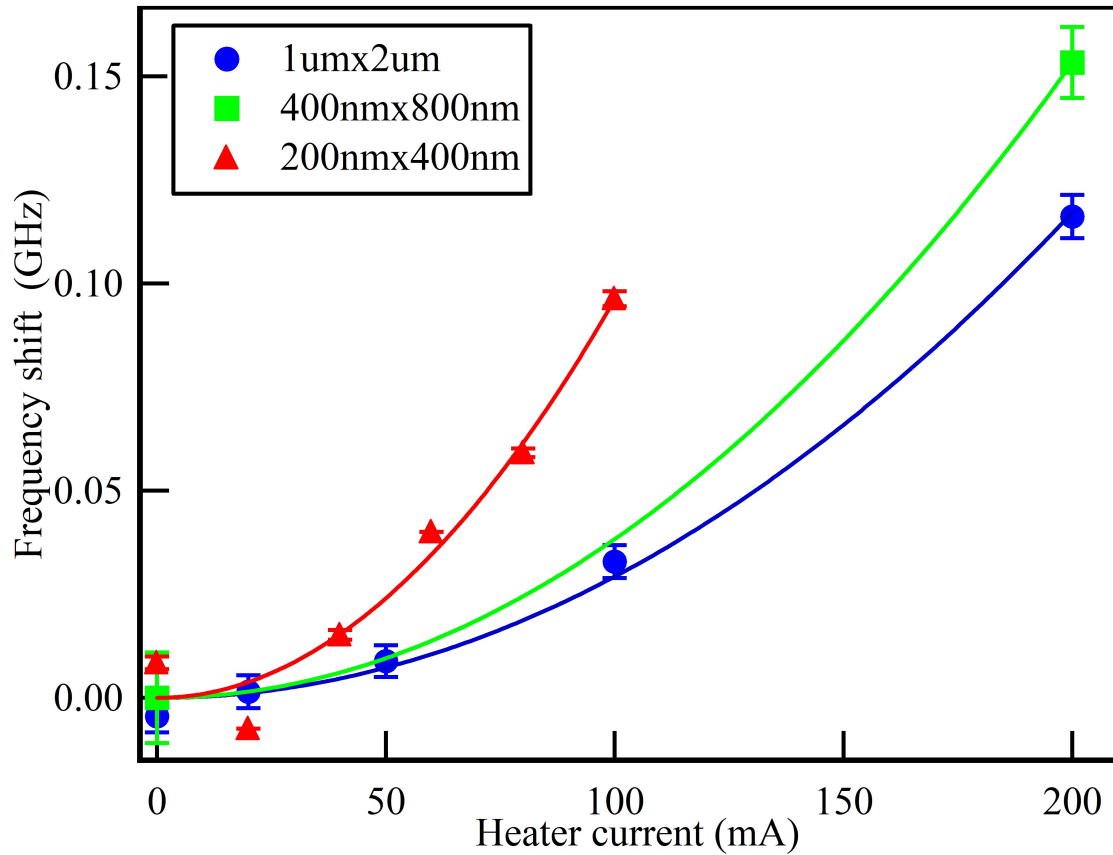


Figure 4.11: Heater current vs frequency shift for various NiFe dot sizes. We can see that smaller dots are causing better spin injection

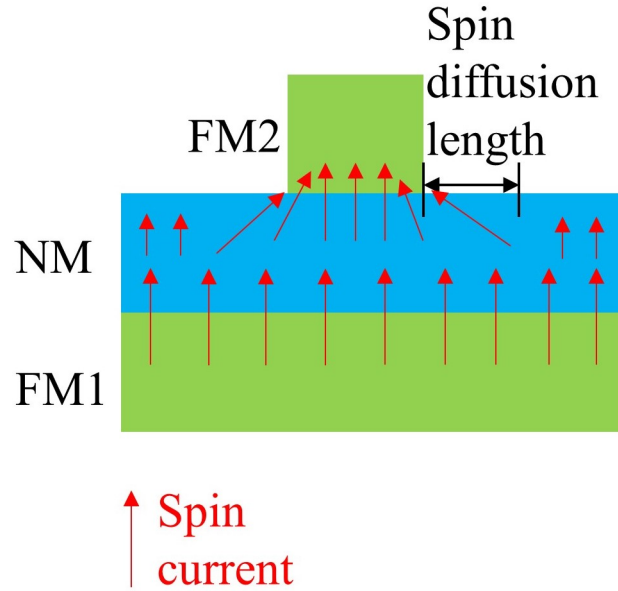


Figure 4.12: A qualitative explanation of dot size dependence of spin injection efficiency. Apart from the spin current that is directly coming from below, NiFe dots also absorb a current from a radius of spin diffusion length in Cu around them.

quency and linewidth, caused by field-like and damping-like torques respectively. The modified FMR frequency will be given by

$$\omega^2 = \gamma^2 (\mu_0 H_{\text{ext}} + b + N_x M_s) (\mu_0 H_{\text{ext}} + b + N_y M_s) \quad (4.3)$$

and the modified linewidth is given by

$$\Delta\omega = \Delta\omega_0 - 2\gamma a \quad (4.4)$$

Upon parabolic fit as shown in figure 4.10, we can extract the parameters a and b , and estimate the ratio of a/b to be approximately -2.5 at any given applied field. This indicates that the field-like torque is significant compared

to the damping-like torque and cannot be ignored.

4.4.1 Dependence on dot-size

Ferromagnets are strong spin absorbers. This means that spin current injected into NiFe dots is not only the current injected from the part of the CoFeAl directly below them, but also includes an area within λ_{sd}^{Cu} around it as shown in figure 4.12. This means that when the dots are made smaller, keeping the dot density (total area of dots/total area of CFA) constant, the spin current density is larger. Figure 4.11 shows how the change in frequency $\Delta\omega$ depends on the dot size. This is consistent with our prediction that smaller dots improve the density of injected spin current.

4.5 Summary

In summary, we investigated the influence of thermally generated spin transfer torque on NiFe nanodots. We used external heating to generate thermal gradient across CoFeAl/Cu interface and produce this spin current which creates the subsequent spin transfer torque. The modification of frequency spectra in terms of both linewidth and resonance frequency point to the coexistence of both damping-like and field-like torque. Additionally, the dot size dependency shows the importance of geometry in such devices.

Chapter 5

Experiment 2: Thermal Spin valve effect

5.1 Introduction

The discovery of Giant Magnetoresistance(GMR)[12, 13] is said to be a very important breakthrough in the field of computer memories. In addition to being used as a memory cell[55], GMR based devices could also be used as magnetic read-heads[56], isolation devices[57] and magnetic field sensors[58]. More recently, GMR was employed in bio-sensor applications[59, 60]. Over the course of time, significant advances were made in the field of spintronics and devices such as lateral spin valve[61] became popular. A new branch of spintronics known as spin-caloritronics, where the interaction between spin and heat is studied, recently became an active area of research[20]. The discovery of the spin Seebeck effect[62] started a wave of research into this field. Very soon, several new effects such as spin-dependent Seebeck effect[63, 48],

spin-Peltier effect[64, 65] and various Nernst effects in ferromagnets[66, 67, 68, 69] were discovered.

However, most of the advances in spin-caloritronics focus on manipulation of spin current using heat, or conversion of heat current into spin current. It is uncommon to study the manipulation of heat current using spins. Heikkil et al[70] have theoretically emphasized this and also predicted violations of Wiedemann-Franz law. So far, Sato et al[71] and Jeong et al[72] have reported field-dependent thermal conductivity in magnetic multilayers. However, a quantitative comparison of thermal and electrical versions of GMR still needs to be done. Additionally, because of the large size, the presence of domains in their samples complicates the analysis and prevents us from making any implications about Wiedemann-Franz law. Recently Bakker et al[1] have developed a useful technique to study the heat transport in nanowires. Using this method, we studied the heat transport in GMR nanowires upon Joule heating by Pt wires and detection using Seebeck effect.

5.2 Sample structure

A schematic of the device is shown in figure 5.1. The object of study is a long, thin GMR wire, 400nm thick and $2\mu\text{m}$ long made of Ferromagnet(FM)/Nonmagnet(NM)/Ferromagnet(FM) trilayer. The NM was always Cu, but the FM was either Co or NiFe. This was made on a SiO_2/Si substrate. On the GMR wire, we made long vertical bars of Pt which are 20nm

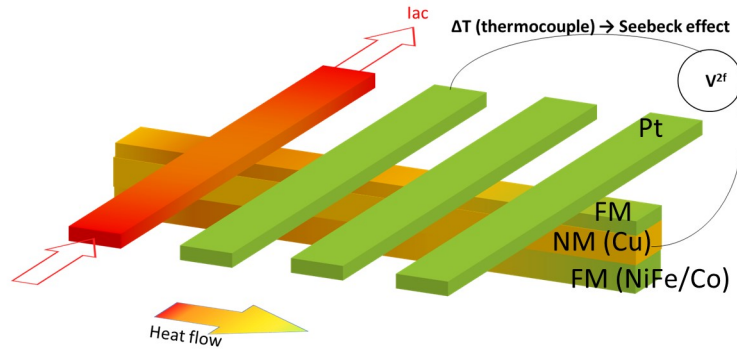


Figure 5.1: A schematic of the device

thin and 400nm wide. The Pt wire both acts as a heating element and a thermometer by forming a thermocouple with the GMR wire. The gap between two Pt wires is 400nm.

- **Device 1:** The GMR wire is made of NiFe/Cu/NiFe of thicknesses 15nm/20nm/5nm respectively. The SiO₂ layer in the substrate is 100nm thick. The NiFe is Ni:Fe in the ratio 80:20.
- **Device 2:** The GMR wire is made of Co/Cu/Co of thicknesses 20nm/10nm/10nm respectively. The SiO₂ layer in the substrate is 1μm thick.

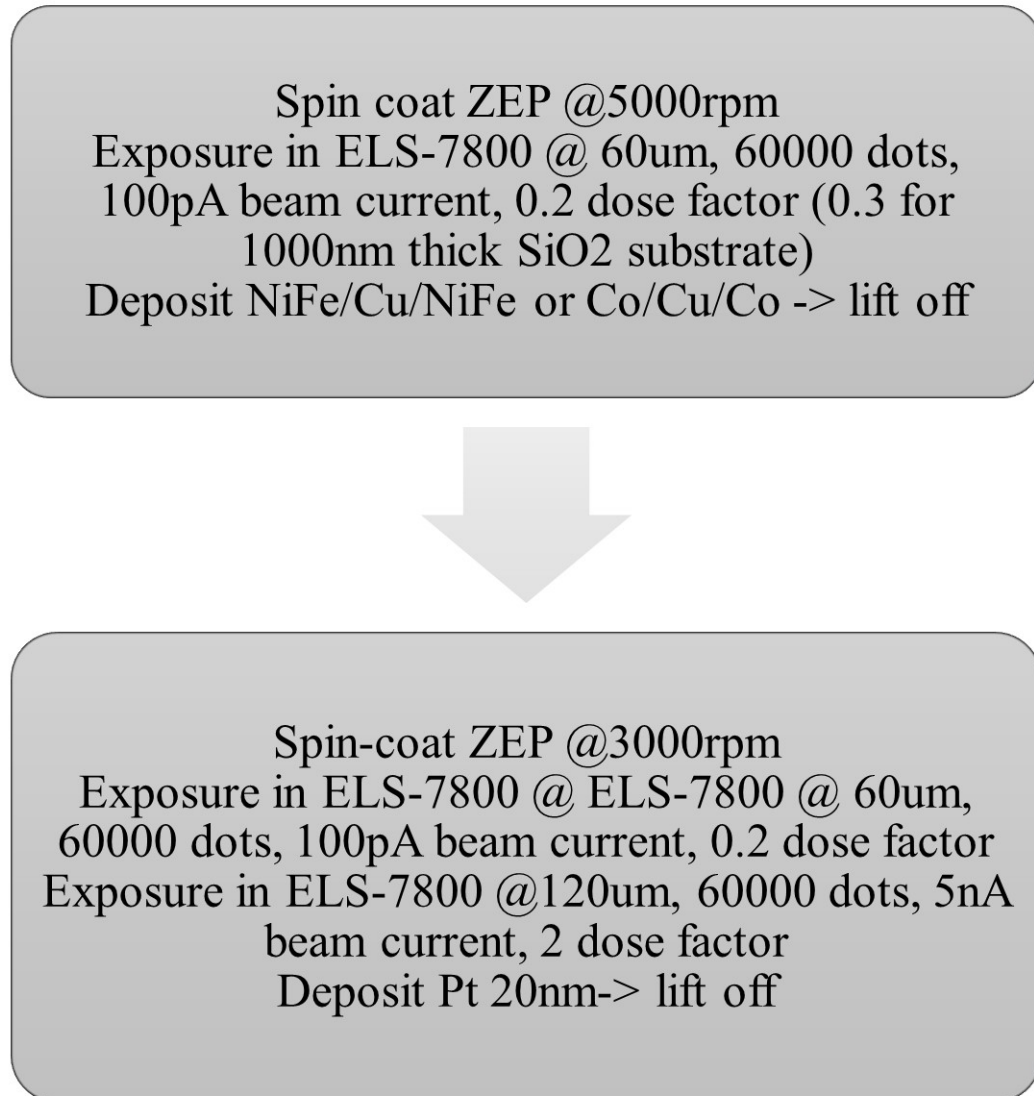


Figure 5.2: Fabrication steps

Figure 5.2 shows the fabrication steps.

5.3 Experiment details

First, we measured the electrical GMR by passing low frequency AC current between Pt1 and Pt4 and measuring the lock-in voltage between Pt2 and Pt3.

After measuring the electrical GMR, a low frequency AC current of frequency 173Hz is passed through the Pt1 wire. This causes Joule heating in the Pt1 wire, which generates a horizontal thermal gradient across the GMR wire. The heat flow through the GMR wire, which is dependent on the thermal conductivity, creates a small additional temperature at the junctions of Pt2, Pt3 and Pt4 with the GMR wire. Then, we measured the second harmonic of the voltage generated at Pt2, Pt3 and Pt4. Since Joule heating is proportional to the square of the current flowing through the Pt1 wire, the effect of Joule heating will be seen as a second harmonic. By separating the second harmonic using lock-in measurement, we can eliminate the possible spurious non-thermal contributions.

We do this procedure for both device 1 and device 2. All measurements were performed at room temperature.

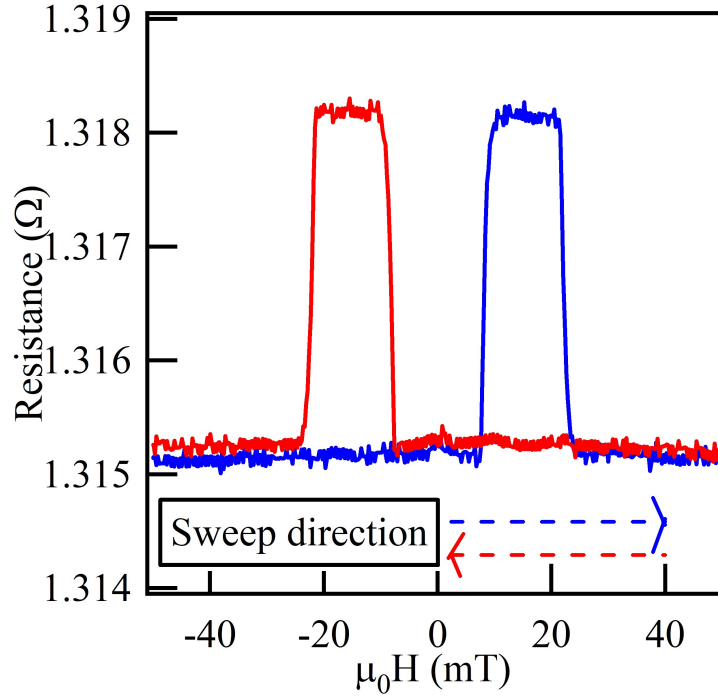


Figure 5.3: Electrical GMR of NiFe/Cu/NiFe

5.4 Results and Discussion

5.4.1 NiFe/Cu/NiFe

Figure 5.3 shows the electrical GMR. Because of the difference in thicknesses, the top layer and the bottom layer switch at different magnetic fields. Thus, we can see different resistances for parallel and anti-parallel magnetization configurations. From this, we can calculate the electrical GMR from the expression

$$\text{GMR} = \frac{R_{AP} - R_P}{R_P} \quad (5.1)$$

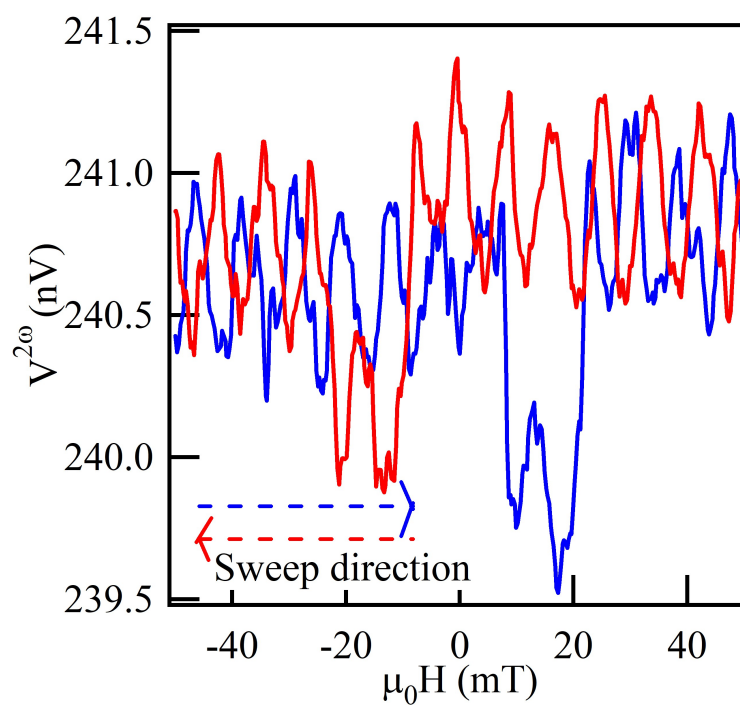


Figure 5.4: Seebeck Voltage at Pt2 of NiFe/Cu/NiFe device showing thermal GMR

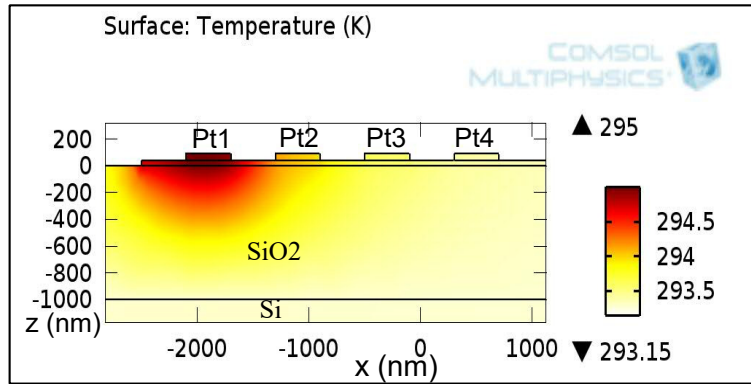


Figure 5.5: Result of COMSOL simulation showing a significant increase in the temperature

as 0.3%. Figure 5.4 shows the Seebeck voltage measured at the terminal Pt2 upon flowing Joule heating current through Pt1. We can see that this too shows a qualitatively similar switching to that of the electrical version. The switching fields show similar values to that of electrical GMR. For a quantitative estimate of the thermal conductivity κ , we have the same problem as that of the above. In addition to the above discussed problem of l , there is also a significant amount of heat draining into the substrate. To take account of all of these, we use the same approach using simulation results from COMSOL Multiphysics software.

Figure 5.5 shows the temperature distribution arising from Joule heating. Please note that we have set the temperature at the bottom of the substrate to be always at room temperature and also used a smaller substrate of the same thickness. This is to avoid the computing time of several days. From the simulation, we plotted the estimated additional temperature ΔT_{Pt2} in

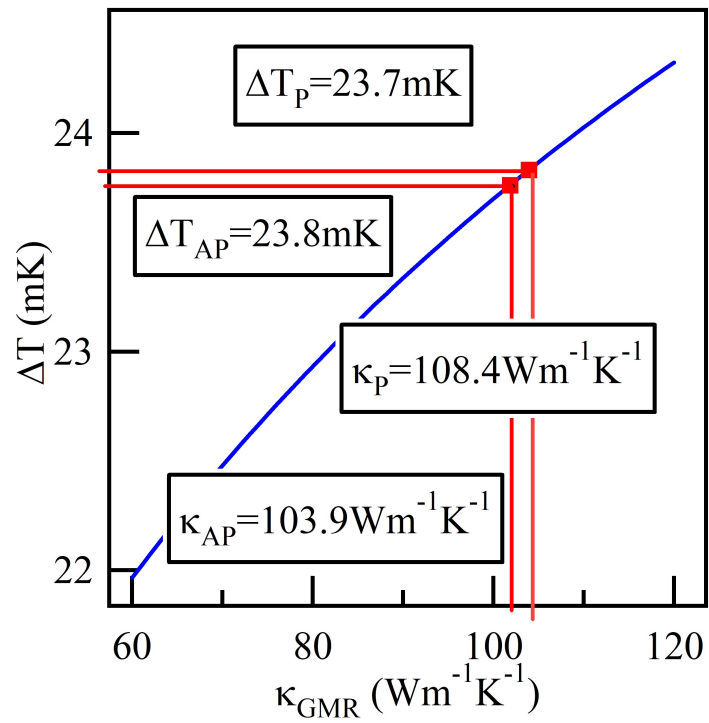


Figure 5.6: Results of COMSOL simulation of NiFe/Cu/NiFe device and extraction of κ

figure 5.6.

By setting the value of $S_{\text{trilayer-Pt}}$ to be $10.1\mu\text{V}/\text{K}$ based on the background signal at different points along the GMR wire, we estimated the corresponding ΔT_{Pt2} for P and AP configurations. We then looked up the corresponding value of κ which would have generated the ΔT_{P} and ΔT_{AP} . Thus, we can obtain the values of κ_{P} and κ_{AP} to be $108.4\text{Wm}^{-1}\text{K}^{-2}$ and $103.9\text{Wm}^{-1}\text{K}^{-2}$ respectively. From this, we can measure the thermal GMR ratio to be approximately 4.3%, which is much higher than the electrical GMR.

5.4.2 Co/Cu/Co

In device 2, the NiFe/Cu/NiFe was changed to Co/Cu/Co because the latter was known to generate large GMR ratio arising from stronger spin-dependent scattering at the interface[73]

Figure 5.7 shows the electrical GMR for Co/Cu/Co. Using the average values of R_{P} and R_{AP} we can calculate the GMR ratio from equation 5.1 as $\approx 1\%$. As expected, this is a significant improvement from NiFe/Cu/NiFe.

Figure 5.8 shows the Seebeck voltage at the Pt2 for device 2. Again, there was a clear difference between parallel and anti-parallel configurations. More importantly, using a thicker SiO_2 resulted in a much higher base voltage S_0 , thereby enabling better signal to noise ratio. The plot of κ vs ΔT is shown in figure 5.9. The values of κ_{P} and κ_{AP} were found to be $58.9\text{Wm}^{-1}\text{K}^{-2}$ and

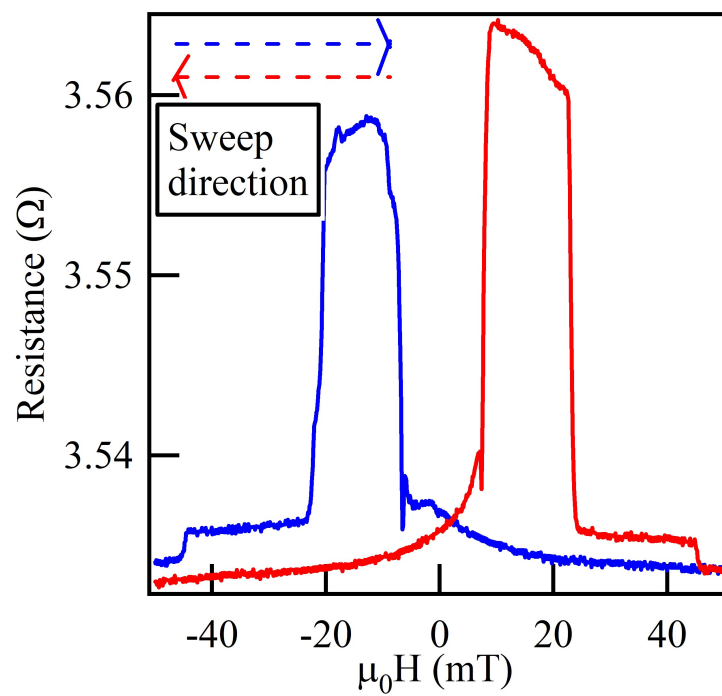


Figure 5.7: Electrical GMR of Co/Cu/Co

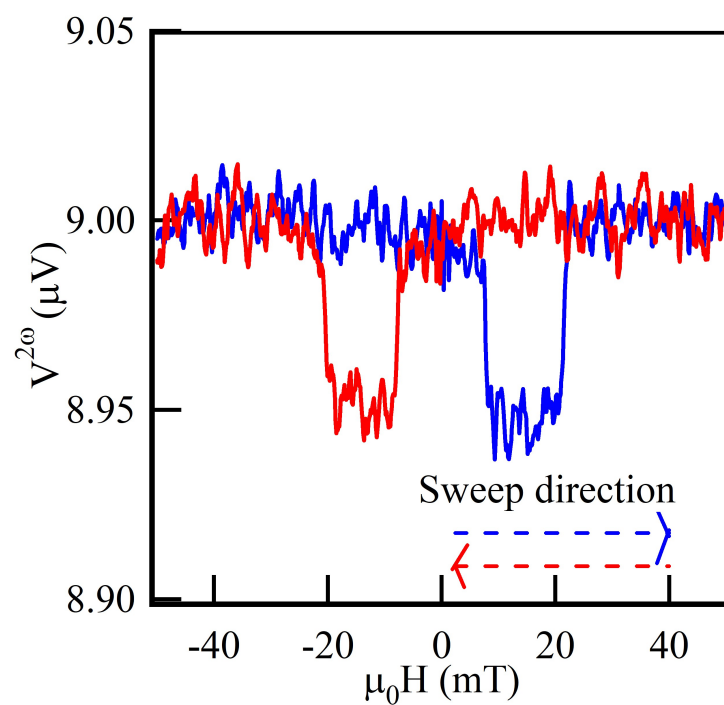


Figure 5.8: Seebeck Voltage at Pt2 of Co/Cu/Co device showing thermal GMR

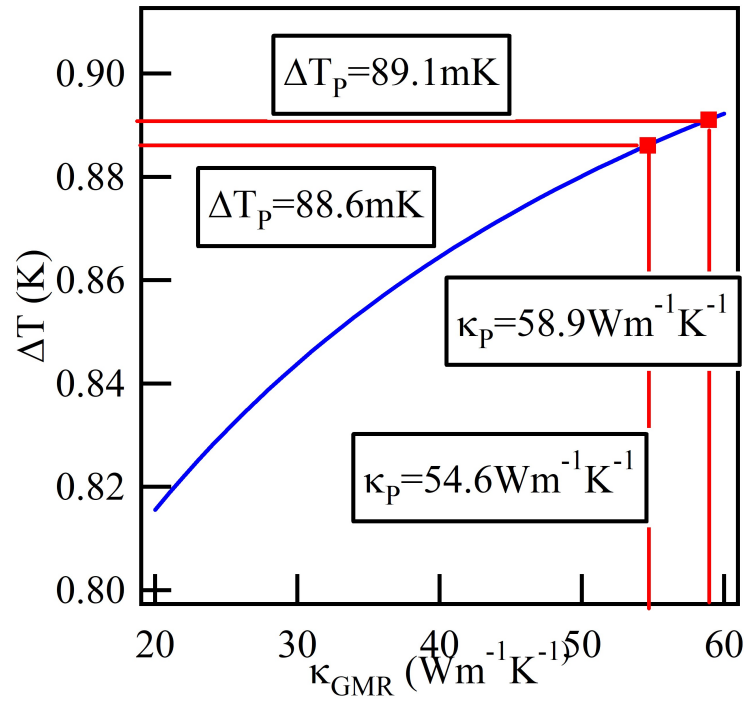


Figure 5.9: Results of COMSOL simulation of Co/Cu/Co device and extraction of κ

$54.6\text{Wm}^{-1}\text{K}^{-2}$ respectively. Thus, Co/Cu/Co also shows a thermal GMR ratio of $(\kappa_{\text{P}} - \kappa_{\text{AP}})/\kappa_{\text{P}}$ as 7.9% which is again much higher than the electrical version.

5.5 Summary

In summary, we investigated the thermal transport in GMR nanowires using a new nanoscale heat sensing technique using Seebeck effect. We used NiFe/Cu/NiFe and Co/Cu/Co nanowires, both of which showed clear magnetoresistance in thermal and electrical signals. By combining this with numerical estimate from COMSOL simulations, we were able to obtain the values of magnetoresistance for electrical and thermal transports. Surprisingly, we found that the thermal conductivity shows a much larger MR ratio than the electrical GMR.

Chapter 6

Experiment 3: Anomalous thermal Hall effect

6.1 Introduction

The discovery of Hall effect[29] in 1879 in normal metals is a starting point for the subsequent several effects of similar fundamental origin in ferromagnetic metals. Anomalous Hall effect[30] which was discovered by Hall himself two years later, received new attention after 100 years[74, 31] since nanoscale devices became ubiquitous and measurement methods were modernized. Falling into the same class of effects are spin Hall effect[75, 76, 77], spin injection Hall effect[78], quantum spin Hall effect[79, 80] and so on.

Spin-caloritronics is a new branch of spintronics in which the interaction between spin and heat is studied[20]. One of the hot areas of research in spin-caloritronics is discovery of various thermoelectric versions of the above

mentioned Hall effects. Nernst effect, which is found in the presence of a magnetic field in paramagnetic metals[81], was discovered long ago. Anomalous Nernst effect, on the other hand, has been receiving a lot of attention recently[82, 83]. However, this class of thermoelectric effects is often mixed up with other signals, leading to difficulty in quantitative analysis[84]. Also, the interfacing ferromagnets and nonmagnets, especially heavy metals, results in still more interfering effects such as ferromagnetic proximity effect[85] and Dzyaloshinskii-Moriya interaction(DMI)[86, 87]. In addition to thermoelectric effects, the thermal(heat current) version of Hall effects has also been researched. Thermal Hall effect was shown in Copper[88], and anomalous thermal hall effect was shown in anti-ferromagnetic MnSn_3 by Li et al[89] and in potassium by Tausch et al[90]. In the light of renewed interest in spin-caloritronic Hall effects, Xu et al[91] theoretically predicted anomalous thermal Hall effect in ferromagnets.

Lateral spin valve[61] in a non-local configuration[92, 41] is a way to generate pure spin current in metallic nanostructures. Using the same device structure, thermally driven spin injection[48] is made possible. However, even here additional contribution from the interplay of Seebeck effect and Peltier effect is observed as a background signal[93]. Furthermore, anomalous Nernst effect has been shown to cause an asymmetry[94, 95] in the thermal spin injection signal. Using the new material CoFeAl which generates a large thermal spin valve signal[49], we made a lateral spin valve to carefully study the interplay of different spin-caloritronic effects in the non-local configuration.

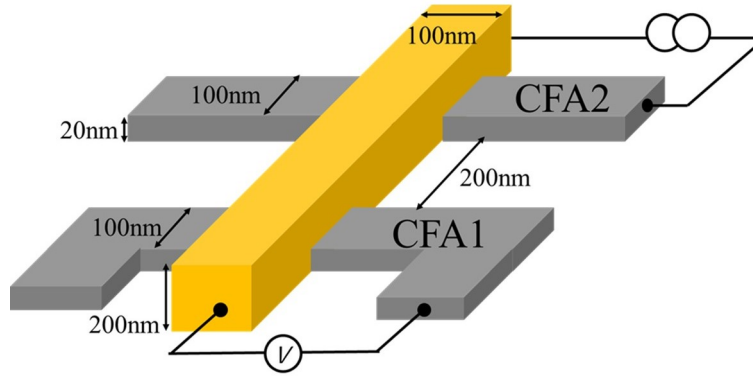


Figure 6.1: A schematic of the device

6.2 Sample structure

Figure 6.1 shows a schematic of the device. The geometry of the device is the same as that of the standard local spin valve that has been previously optimized. [49, 50]. There are two long, thin vertical bars of a CoFeAl (CFA) of thickness either 20nm or 50nm and width 100nm, which are joined by a 200nm thick, 100nm wide Cu channel. The large Cu thickness is to generate a larger thermal gradient across Cu/CoFeAl junction. The center-to-center distance of the two CoFeAl bars was 300nm, which is substantially smaller than the spin diffusion length in Cu. The coercivity of one of the CoFeAl bars was changed by changing the shape. Two small pads are added at the ends, which makes the switching easier, therefore the switching field was smaller. The fabrication steps are shown in the figure 6.2

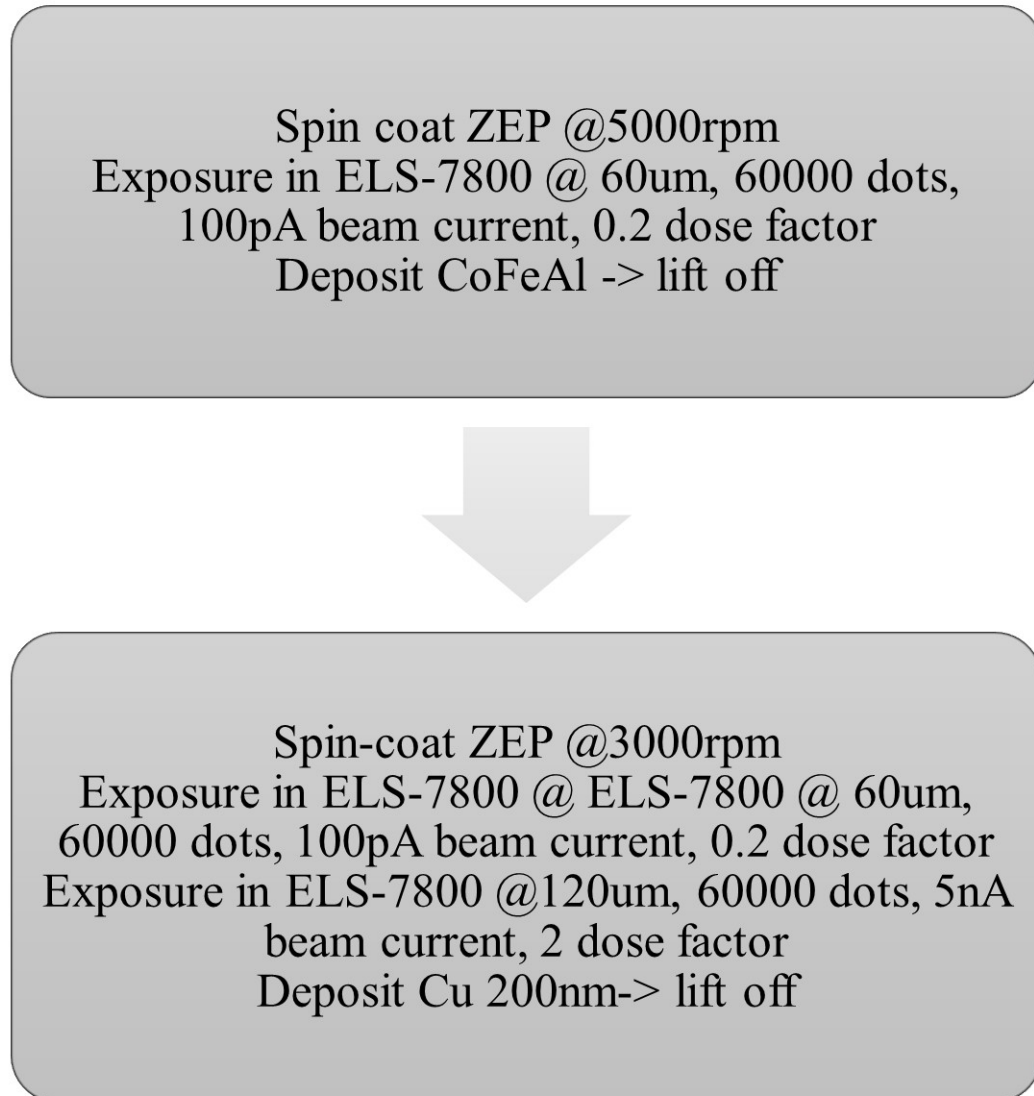


Figure 6.2: Fabrication steps

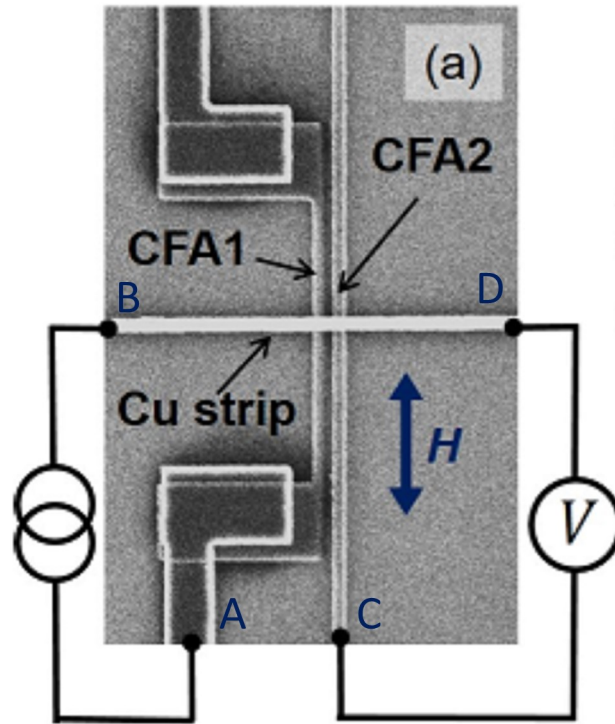


Figure 6.3: Measurement configuration

6.3 Measurement

Figure 6.3 shows the measurement technique. In this experiment, to generate pure spin current, non-local measurement method was employed. Current I_{in} is flown between terminals A and B as shown in the figure and voltage V_{out} is measured between terminals C and D . Thus, CFA1 becomes the injector and CFA2 becomes the detector. Now, we used lock-in measurement and measured the first harmonic(1ω) of the V_{out} for the conventional electrical measurement and the second harmonic(2ω) for thermal signal. The fact that Joule heating is proportional to I_{in}^2 causes the thermal signal to ap-

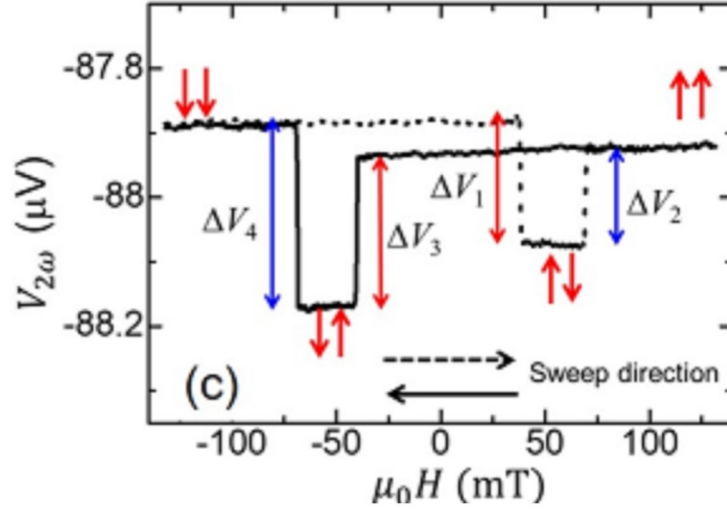


Figure 6.4: Thermal signal from device 1

pear as the second harmonic.

6.4 Results and discussion

Initially, we made the device with a CoFeAl thickness of 20nm. We confirmed that the device behaved as expected by measuring the electrical spin injection signal as the first harmonic of V_{out} . Then, we measured the second harmonic signal, which showed a thermal signal as expected. This is shown in figure 6.4. There are two predominant contributions to this signal. First is the spin-valve-like switching which comes from the thermal spin injection from CFA1 and detection at CFA2. Second is the background signal V_{Seebeck} that comes from the heat that is generated at the injector and then flows

through the Copper channel to CFA2, which ultimately generates Seebeck voltage between CFA2 and Cu.

But, these two effects alone cannot explain the asymmetry. This asymmetry is supposed to be caused by the anomalous Nernst effect. Anomalous Nernst effect is the thermoelectric effect in ferromagnets where a thermal gradient produces a perpendicular voltage. This is the thermoelectric analog of Hall effect and has similar origins. Since the heat flow at Cu/CFA2 interface is mainly vertical and CFA2 is a ferromagnet, there was a small voltage created perpendicular because of the anomalous Nernst effect. And because the voltage generated depends on the magnetization of the CFA2, this caused an asymmetry in the thermal signal.

However, this picture is not complete. Let us call the differences in voltage whenever there is a magnetization reversal (switching) as ΔV_1 , ΔV_2 , ΔV_3 and ΔV_4 as shown in figure 6.4. The switching at a higher field ΔV_2 and ΔV_4 are caused by the switching of CFA2, which is the detector. But ΔV_1 and ΔV_3 are caused by switching at the injector CFA1. Hence, the difference $\Delta V_1 - \Delta V_3$ cannot be explained by the anomalous Nernst effect.

In order to explain this, we looked at the geometry of the spin-valve device more closely. As shown in figure 6.5, the Cu channel surrounds the CoFeAl bar because of the fabrication process. Although the dominant thermal gradient ΔT_z is vertical (along z-axis) because of the large Cu channel, anomalous thermal Hall effect causes a small lateral heat current. This lat-

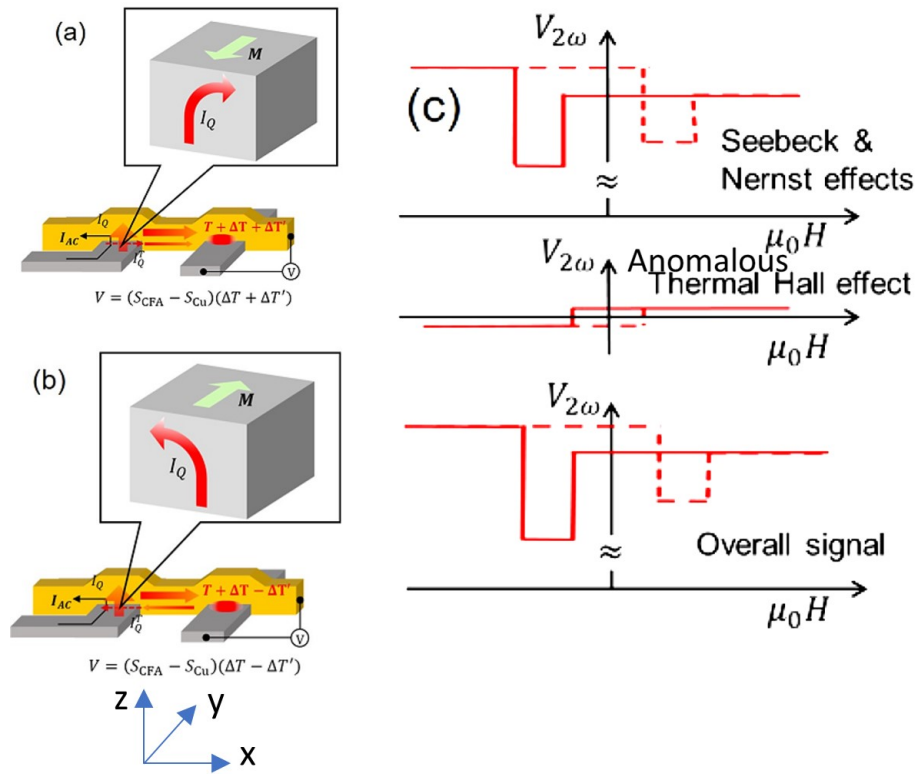


Figure 6.5: Explanation of the interaction of three different effects in device

eral heat current then contributes to the background signal V_{Seebeck} . Since the anomalous thermal hall effect also depends on the magnetization direction of the ferromagnet, a switch in CFA1 induces change in V_{Seebeck} . This causes a difference between ΔV_1 and ΔV_3 , thus completing the picture. Figure 6.5 explains qualitatively how the interplay of three signals (1) thermal spin injection, (2) anomalous Nernst effect and (3) anomalous thermal Hall effect result in the overall signal that we measured.

6.4.1 Upon reversing the roles of injector and detector

To measure the thermal hall effect more clearly, we needed to enhance the sideways contribution to the overall signal. Hence, we made a new device with a thicker CoFeAl of 50nm. We repeated the above process and found that the asymmetry was even more pronounced.

After getting a clearer signal, we did the experiment once again with the injector and detector reversed. That is, current I_{in} was flowed through CFA2 and voltage was detected at CFA1. As expected, this causes a change in the second harmonic lock-in signal as shown in figure 6.6. Let us call the injector-detector configurations in figure 6.6 as P and Q respectively. In both configurations P and Q , asymmetries were observed as $\Delta V_1 < \Delta V_3$ and $\Delta V_2 < \Delta V_4$. However, the magnitude of asymmetry is different between P and Q . In configuration P , $\Delta V_3 - \Delta V_1$ is caused by anomalous thermal Hall effect and $\Delta V_4 - \Delta V_2$ by anomalous Nernst effect. In configuration Q , $\Delta V_4 - \Delta V_2$ is caused by anomalous thermal Hall effect and $\Delta V_3 - \Delta V_1$ is caused by

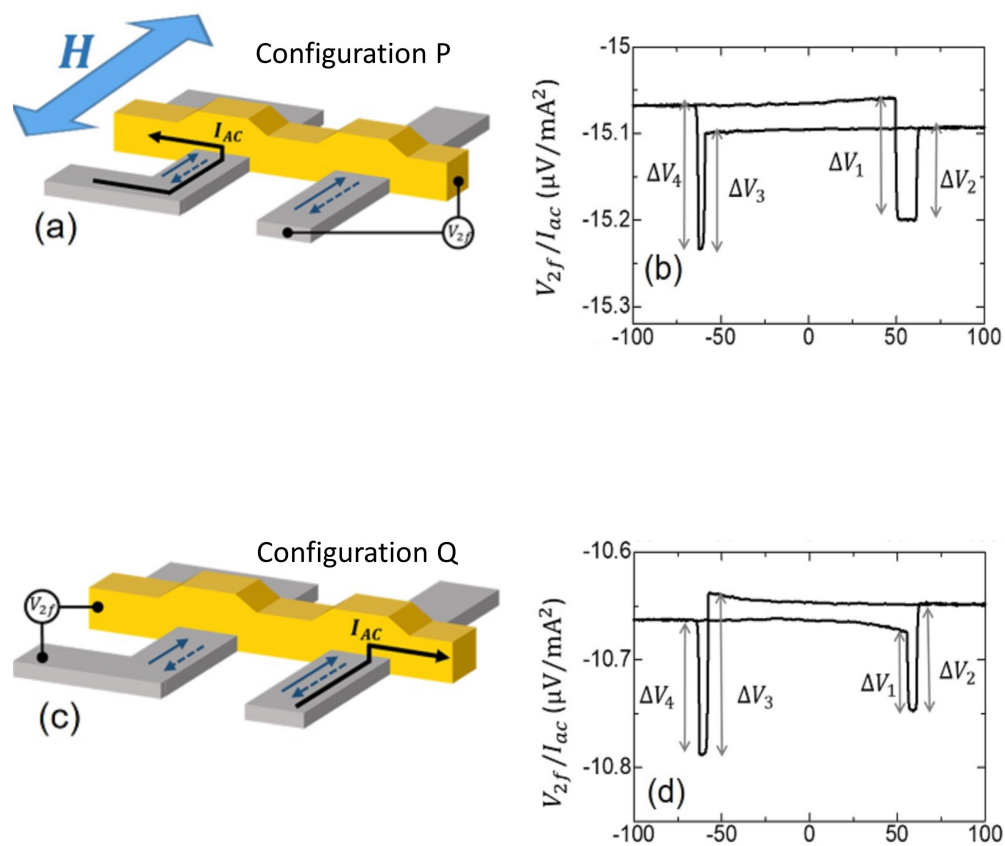


Figure 6.6: Dependence on probe configuration

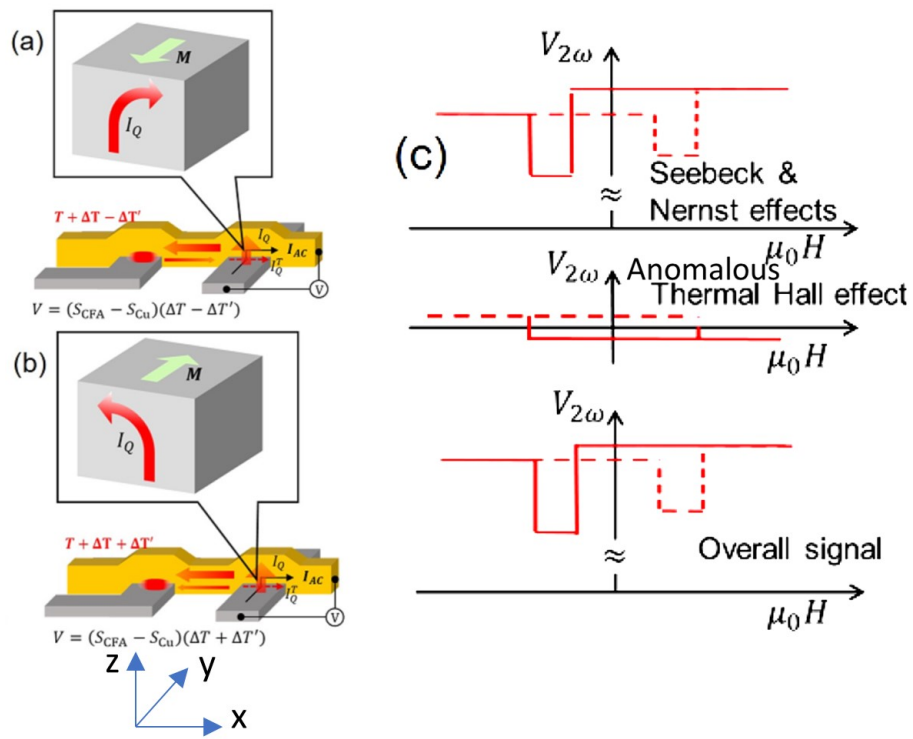


Figure 6.7: Explanation of the signal in configuration B

anomalous Nernst effect. As we have seen previously, the contribution, from anomalous thermal hall effect is smaller which causes the difference of signals from configurations P and Q . This is consistent with our initial hypothesis.

6.5 Summary

In summary, we undertook a careful exploration of the reasons for asymmetry in the thermal spin injection signal in the lateral spin-valve in nonlocal configuration. After a detailed analysis of the signal with enhanced sideways contribution, we concluded that the asymmetry is caused by the combination of anomalous Nernst effect and anomalous thermal Hall effect. This shows the importance of careful understanding of Hall-effect like signals in nanoscale thermal transport.

Chapter 7

Summary

To summarize, we experimentally verified the thermal analogues of three different spintronic effects, namely spin transfer torque, Giant Magnetoresistance(GMR) and Anomalous Hall effect.

First, we investigated the effect of thermally generated spin transfer torque on NiFe nanodots. For this purpose, we used a trilayer made of NiFe/Cu/CoFeAl. The top NiFe layer was patterned into small dots for spin injection efficiency. We used a W heater to create a vertical thermal gradient and a Cu co-planar waveguide to measure the ferromagnetic resonance (FMR) using vector network analyzer (VNA). The VNA-FMR signal shows a clear dependence of dynamics on the thermal spin injection, implying evidence for spin transfer torque. We found that both linewidth and resonance frequency are altered, which means that both damping-like torque and field-like torque are present.

Then, we studied the flow of heat current in GMR nanowires by using a novel heat sensing technique using Seebeck effect. As expected thermal GMR was found and the material dependence is similar to that of electrical GMR attuning to the strong correlation of electrical and thermal transport in metals. However, an unexpected effect was found, which is that the thermal GMR is much larger than the electrical GMR.

Finally, we analyzed the asymmetric thermal spin injection signal in the lateral spin valves in the nonlocal configuration. We found that the interplay of anomalous Nernst effect and the anomalous thermal Hall effect is the reason for the asymmetry.

In all, we studied various effects of temperature gradient across ferromagnet/nonmagnet heterostructures and found experimental evidence for thermal spin transfer torque, thermal GMR and anomalous thermal Hall effect.

Given the newly found importance of spin-caloritronics and the renewed focus on heat-to-spin conversion techniques, a good understanding of the link between thermal and electrical transport mechanisms is necessary. Putting the above research next to a good amount of existing evidence for thermoelectric analogues of spintronic effects, as long as we don't go 'quantum', we can conclusively say that any new finding in electrical transport can be expected to be replicated in the thermal and thermoelectric versions and vice versa.

Bibliography

- [1] F. L. Bakker, J. Flipse, and B. J. Van Wees, “Nanoscale temperature sensing using the Seebeck effect,” *Journal of Applied Physics*, vol. 111, no. 8, 2012.
- [2] G. Chen and A. Shakouri, “Heat Transfer in Nanostructures for Solid-State Energy Conversion,” *Journal of Heat Transfer*, vol. 124, p. 242, apr 2002.
- [3] D. G. Cahill, W. K. Ford, K. E. Goodson, G. D. Mahan, A. Majumdar, H. J. Maris, R. Merlin, and S. R. Phillpot, “Nanoscale thermal transport,” *Journal of Applied Physics*, vol. 93, pp. 793–818, jan 2003.
- [4] D. G. Cahill, P. V. Braun, G. Chen, D. R. Clarke, S. Fan, K. E. Goodson, P. Keblinski, W. P. King, G. D. Mahan, A. Majumdar, H. J. Maris, S. R. Phillpot, E. Pop, and L. Shi, “Nanoscale thermal transport. II. 20032012,” *Applied Physics Reviews*, vol. 1, p. 011305, mar 2014.
- [5] A. A. Cohen, “Technical Developments: Magnetic Drum Storage for Digital Information Processing Systems,” *Mathematical Tables and Other Aids to Computation*, vol. 4, p. 31, jan 1950.

- [6] A. Wang and W. D. Woo, "Static Magnetic Storage and Delay Line," *Journal of Applied Physics*, vol. 21, pp. 49–54, jan 1950.
- [7] L. D. Stevens, "The Evolution of Magnetic Storage," *IBM Journal of Research and Development*, vol. 25, pp. 663–676, sep 1981.
- [8] T. Shinjo, *Nanomagnetism and spintronics*. Elsevier, 2009.
- [9] J.-i. Inoue, "GMR, TMR and BMR," *Nanomagnetism and Spintronics*, pp. 15–92, jan 2009.
- [10] J.-G. J. Zhu and C. Park, "Magnetic tunnel junctions," *Materials Today*, vol. 9, pp. 36–45, nov 2006.
- [11] R. F. C. Farrow, S. S. P. Parkin, P. J. Dobson, J. H. Neave, and A. S. Arrott, eds., *Thin Film Growth Techniques for Low-Dimensional Structures*, vol. 163 of *NATO ASI Series*. Boston, MA: Springer US, 1987.
- [12] M. N. Baibich, J. M. Broto, A. Fert, F. N. Van Dau, F. Petroff, P. Eitenne, G. Creuzet, A. Friederich, and J. Chazelas, "Giant magnetoresistance of (001)Fe/(001)Cr magnetic superlattices," *Physical Review Letters*, vol. 61, no. 21, pp. 2472–2475, 1988.
- [13] G. Binasch, P. Grünberg, F. Saurenbach, and W. Zinn, "Enhanced magnetoresistance in layered magnetic structures with antiferromagnetic interlayer exchange," *Physical Review B*, vol. 39, no. 7, pp. 4828–4830, 1989.
- [14] "The 2007 Nobel Prize in Physics - Press release."

- [15] S. S. Maekawa, S. O. Valenzuela, E. Saitoh, and K. Kimura, *Spin current*. Oxford Science Publications, 2012.
- [16] S. Takahashi and S. Maekawa, “Spin Current in Metals and Superconductors,” *Journal of the Physical Society of Japan*, vol. 77, p. 031009, mar 2008.
- [17] J. Slonczewski, “Current-driven excitation of magnetic multilayers,” *Journal of Magnetism and Magnetic Materials*, vol. 159, pp. L1–L7, jun 1996.
- [18] S. Zhang, P. M. Levy, and A. Fert, “Mechanisms of Spin-Polarized Current-Driven Magnetization Switching,” *Physical Review Letters*, vol. 88, p. 236601, may 2002.
- [19] D. Apalkov, B. Dieny, and J. M. Slaughter, “Magnetoresistive Random Access Memory,” *Proceedings of the IEEE*, vol. 104, pp. 1796–1830, oct 2016.
- [20] G. E. Bauer, E. Saitoh, and B. J. Van Wees, “Spin caloritronics,” *Nature Materials*, vol. 11, pp. 391–399, may 2012.
- [21] A. Jain and A. J. H. McGaughey, “Thermal transport by phonons and electrons in aluminum, silver, and gold from first principles,” *Physical Review B*, vol. 93, p. 081206, feb 2016.
- [22] N. W. Ashcroft and N. D. Mermin, *Solid state physics*. Holt, Rinehart and Winston, 1976.

- [23] E. Y. E. Y. Tsymbal and I. Zutic, *Handbook of spin transport and magnetism*. CRC Press, 2012.
- [24] W. Thomson, “On the Electro-Dynamic Qualities of Metals:—Effects of Magnetization on the Electric Conductivity of Nickel and of Iron,” *Proceedings of the Royal Society of London*, vol. 8, pp. 546–550, jan 1856.
- [25] T. McGuire and R. Potter, “Anisotropic magnetoresistance in ferromagnetic 3d alloys,” *IEEE Transactions on Magnetism*, vol. 11, pp. 1018–1038, jul 1975.
- [26] B. Dieny, V. S. Speriosu, S. S. Parkin, B. A. Gurney, D. R. Wilhoit, and D. Mauri, “Giant magnetoresistive in soft ferromagnetic multilayers,” *Physical Review B*, vol. 43, pp. 1297–1300, jan 1991.
- [27] D. Thompson, L. Romankiw, and A. Mayadas, “Thin film magnetoresistors in memory, storage, and related applications,” *IEEE Transactions on Magnetism*, vol. 11, pp. 1039–1050, jul 1975.
- [28] T. Valet and A. Fert, “Theory of the perpendicular magnetoresistance in magnetic multilayers,” *Physical Review B*, vol. 48, pp. 7099–7113, sep 1993.
- [29] E. H. Hall, “On a New Action of the Magnet on Electric Currents,” *American Journal of Mathematics*, vol. 2, p. 287, sep 1879.
- [30] E. Hall, “XVIII. *<i>On the Rotational Coefficient in nickel and cobalt</i>*,” *The London, Edinburgh, and Dublin Philosophical Magazine and Journal of Science*, vol. 12, pp. 157–172, sep 1881.

- [31] N. Nagaosa, J. Sinova, S. Onoda, A. H. MacDonald, and N. P. Ong, “Anomalous Hall effect,” *Reviews of Modern Physics*, vol. 82, pp. 1539–1592, may 2010.
- [32] M. V. Berry, “Quantal Phase Factors Accompanying Adiabatic Changes,” *Proceedings of the Royal Society A: Mathematical, Physical and Engineering Sciences*, vol. 392, pp. 45–57, mar 1984.
- [33] R. Karplus and J. M. Luttinger, “Hall Effect in Ferromagnetics,” *Physical Review*, vol. 95, pp. 1154–1160, sep 1954.
- [34] C. Kittel, “On the Theory of Ferromagnetic Resonance Absorption,” *Physical Review*, vol. 73, pp. 155–161, jan 1948.
- [35] J. H. Van Vleck, “Concerning the Theory of Ferromagnetic Resonance Absorption,” *Physical Review*, vol. 78, pp. 266–274, may 1950.
- [36] G. Counil, J.-V. Kim, T. Devolder, C. Chappert, K. Shigeto, and Y. Otani, “Spin wave contributions to the high-frequency magnetic response of thin films obtained with inductive methods,” *Journal of Applied Physics*, vol. 95, pp. 5646–5652, may 2004.
- [37] C. Chappert, A. Fert, and F. N. Van Dau, “The emergence of spin electronics in data storage,” *Nature Materials*, vol. 6, pp. 813–823, nov 2007.
- [38] L. Berger, “Emission of spin waves by a magnetic multilayer traversed by a current,” *Physical Review B*, vol. 54, pp. 9353–9358, oct 1996.

- [39] M. Tsoi, A. G. M. Jansen, J. Bass, W.-C. Chiang, M. Seck, V. Tsoi, and P. Wyder, “Excitation of a Magnetic Multilayer by an Electric Current,” *Physical Review Letters*, vol. 80, pp. 4281–4284, may 1998.
- [40] E. B. Myers, D. C. Ralph, J. A. Katine, R. N. Louie, and R. A. Buhrman, “Current-induced switching of domains in magnetic multilayer devices,” *Science (New York, N.Y.)*, vol. 285, pp. 867–70, aug 1999.
- [41] T. Kimura, Y. Otani, and J. Hamrle, “Switching Magnetization of a Nanoscale Ferromagnetic Particle Using Nonlocal Spin Injection,” *Physical Review Letters*, vol. 96, p. 037201, jan 2006.
- [42] J. Sun, “Current-driven magnetic switching in manganite trilayer junctions,” *Journal of Magnetism and Magnetic Materials*, vol. 202, pp. 157–162, jun 1999.
- [43] A. A. Tulapurkar, Y. Suzuki, A. Fukushima, H. Kubota, H. Maehara, K. Tsunekawa, D. D. Djayaprawira, N. Watanabe, and S. Yuasa, “Spin-torque diode effect in magnetic tunnel junctions,” *Nature*, vol. 438, pp. 339–342, nov 2005.
- [44] M. D. Stiles and A. Zangwill, “Anatomy of spin-transfer torque,” *Physical Review B*, vol. 66, p. 014407, jun 2002.
- [45] A. Brataas, A. D. Kent, and H. Ohno, “Current-induced torques in magnetic materials,” *Nature Materials*, vol. 11, pp. 372–381, may 2012.
- [46] J. E. Wegrowe, “Spin transfer from the point of view of the ferromagnetic degrees of freedom,” *Solid State Communications*, vol. 150, pp. 519–523, mar 2010.

- [47] N. Locatelli, V. Cros, and J. Grollier, “Spin-torque building blocks,” *Nature Materials*, vol. 13, pp. 11–20, jan 2014.
- [48] A. Slachter, F. L. Bakker, J.-P. Adam, and B. J. van Wees, “Thermally driven spin injection from a ferromagnet into a non-magnetic metal,” *Nature Physics*, vol. 6, pp. 879–882, nov 2010.
- [49] S. Hu, H. Itoh, and T. Kimura, “Efficient thermal spin injection using CoFeAl nanowire,” *NPG Asia Materials*, vol. 6, p. e127, sep 2014.
- [50] T. Nomura, T. Ariki, S. Hu, and T. Kimura, “Efficient thermal spin injection in metallic nanostructures,” *Journal of Physics D: Applied Physics*, vol. 50, p. 465003, nov 2017.
- [51] M. Hatami, G. E. W. Bauer, Q. Zhang, and P. J. Kelly, “Thermal Spin-Transfer Torque in Magnetoelectronic Devices,” *Physical Review Letters*, vol. 99, p. 066603, aug 2007.
- [52] G.-M. Choi, C.-H. Moon, B.-C. Min, K.-J. Lee, and D. G. Cahill, “Thermal spin-transfer torque driven by the spin-dependent Seebeck effect in metallic spin-valves,” *Nature Physics*, vol. 11, pp. 576–581, jul 2015.
- [53] A. Bose, A. K. Shukla, K. Konishi, S. Jain, N. Asam, S. Bhuktare, H. Singh, D. D. Lam, Y. Fujii, S. Miwa, Y. Suzuki, and A. A. Tulapurkar, “Observation of thermally driven field-like spin torque in magnetic tunnel junctions,” *Applied Physics Letters*, vol. 109, p. 032406, jul 2016.
- [54] S. Petit, C. Baraduc, C. Thirion, U. Ebels, Y. Liu, M. Li, P. Wang, and B. Dieny, “Spin-Torque Influence on the High-Frequency Magnetization

- Fluctuations in Magnetic Tunnel Junctions,” *Physical Review Letters*, vol. 98, p. 077203, feb 2007.
- [55] J. Daughton, “GMR applications,” *Journal of Magnetism and Magnetic Materials*, vol. 192, pp. 334–342, feb 1999.
- [56] Ching Tsang, R. Fontana, Tsann Lin, D. Heim, V. Speriosu, B. Gurney, and M. Williams, “Design, fabrication and testing of spin-valve read heads for high density recording,” *IEEE Transactions on Magnetism*, vol. 30, no. 6, pp. 3801–3806, 1994.
- [57] T. Hermann, W. Black, and S. Hui, “Magnetically coupled linear isolator,” *IEEE Transactions on Magnetism*, vol. 33, no. 5, pp. 4029–4031, 1997.
- [58] J. Daughton, J. Brown, E. Chen, R. Beech, A. Pohm, and W. Kude, “Magnetic field sensors using GMR multilayer,” *IEEE Transactions on Magnetism*, vol. 30, no. 6, pp. 4608–4610, 1994.
- [59] J. Choi, A. W. Gani, D. J. Bechstein, J.-R. Lee, P. J. Utz, and S. X. Wang, “Portable, one-step, and rapid GMR biosensor platform with smartphone interface,” *Biosensors and Bioelectronics*, vol. 85, pp. 1–7, nov 2016.
- [60] D. Hall, R. Gaster, T. Lin, S. Osterfeld, S. Han, B. Murmann, and S. Wang, “GMR biosensor arrays: A system perspective,” *Biosensors and Bioelectronics*, vol. 25, pp. 2051–2057, may 2010.

- [61] M. Johnson and R. H. Silsbee, “Interfacial charge-spin coupling: Injection and detection of spin magnetization in metals,” *Physical Review Letters*, vol. 55, no. 17, pp. 1790–1793, 1985.
- [62] K. Uchida, S. Takahashi, K. Harii, J. Ieda, W. Koshibae, K. Ando, S. Maekawa, and E. Saitoh, “Observation of the spin Seebeck effect,” *Nature*, vol. 455, pp. 778–781, oct 2008.
- [63] M. Johnson and R. H. Silsbee, “Thermodynamic analysis of interfacial transport and of the thermomagnetolectric system,” *Physical Review B*, vol. 35, no. 10, pp. 4959–4972, 1987.
- [64] M. Hatami, G. E. W. Bauer, Q. Zhang, and P. J. Kelly, “Thermoelectric effects in magnetic nanostructures,” *Physical Review B*, vol. 79, no. 17, p. 174426, 2009.
- [65] J. Flipse, F. L. Bakker, A. Slachter, F. K. Dejene, and B. J. Van Wees, “Direct observation of the spin-dependent Peltier effect,” *Nature Nanotechnology*, vol. 7, no. 3, pp. 166–168, 2012.
- [66] H. B. Callen, “The application of onsager’s reciprocal relations to thermoelectric, thermomagnetic, and galvanomagnetic effects,” *Physical Review*, vol. 73, no. 11, pp. 1349–1358, 1948.
- [67] Y. Pu, E. Johnston-Halperin, D. D. Awschalom, and J. Shi, “Anisotropic thermopower and planar Nernst effect in $\text{Ga}_{1-x}\text{Mn}_x\text{As}$ ferromagnetic semiconductors,” *Physical Review Letters*, vol. 97, no. 3, pp. 1–4, 2006.

- [68] Y. Pu, D. Chiba, F. Matsukura, H. Ohno, and J. Shi, “Mott relation for anomalous hall and nernst effects in $\text{Ga}_{1-x}\text{Mn}_x\text{As}$ ferromagnetic semiconductors,” *Physical Review Letters*, vol. 101, no. 11, pp. 1–4, 2008.
- [69] J. Weischenberg, F. Freimuth, S. Blügel, and Y. Mokrousov, “Scattering-independent anomalous Nernst effect in ferromagnets,” *Physical Review B - Condensed Matter and Materials Physics*, vol. 87, no. 6, pp. 1–5, 2013.
- [70] T. T. Heikkilä, M. Hatami, and G. E. W. Bauer, “Spin heat accumulation and its relaxation in spin valves,” *Physical Review B - Condensed Matter and Materials Physics*, vol. 81, no. 10, pp. 1–4, 2010.
- [71] H. Sato, Y. Aoki, Y. Kobayashi, H. Yamamoto, and T. Shinjo, “Huge magnetic field-dependent thermal conductivity in magnetic multilayer films,” *Journal of Magnetism and Magnetic Materials*, vol. 126, no. 1-3, pp. 410–412, 1993.
- [72] T. Jeong, M. T. Moneck, and J. G. Zhu, “Giant magneto-thermal conductivity in magnetic multilayers,” *IEEE Transactions on Magnetics*, vol. 48, pp. 3031–3034, nov 2012.
- [73] S. S. P. Parkin, A. Modak, and D. J. Smith, “Dependence of giant magnetoresistance on Cu-layer thickness in Co/Cu multilayers: A simple dilution effect,” *Physical Review B*, vol. 47, pp. 9136–9139, apr 1993.
- [74] N. A. Sinitsyn, “Semiclassical theories of the anomalous Hall effect,” *Journal of Physics: Condensed Matter*, vol. 20, p. 023201, jan 2008.

- [75] S. O. Valenzuela and M. Tinkham, “Direct electronic measurement of the spin Hall effect,” *Nature*, vol. 442, pp. 176–179, jul 2006.
- [76] J. E. Hirsch, “Spin Hall Effect,” *Physical Review Letters*, vol. 83, pp. 1834–1837, aug 1999.
- [77] S. Zhang, “Spin Hall Effect in the Presence of Spin Diffusion,” *Physical Review Letters*, vol. 85, pp. 393–396, jul 2000.
- [78] J. Wunderlich, A. C. Irvine, J. Sinova, B. G. Park, L. P. Zârbo, X. L. Xu, B. Kaestner, V. Novák, and T. Jungwirth, “Spin-injection Hall effect in a planar photovoltaic cell,” *Nature Physics*, vol. 5, pp. 675–681, sep 2009.
- [79] B. A. Bernevig, T. L. Hughes, and S.-C. Zhang, “Quantum spin Hall effect and topological phase transition in HgTe quantum wells,” *Science (New York, N.Y.)*, vol. 314, pp. 1757–61, dec 2006.
- [80] X.-L. Qi and S.-C. Zhang, “The quantum spin Hall effect and topological insulators,” *Physics Today*, vol. 63, pp. 33–38, jan 2010.
- [81] K. Behnia, “The Nernst effect and the boundaries of the Fermi liquid picture,” *Journal of Physics: Condensed Matter*, vol. 21, p. 113101, mar 2009.
- [82] Y. Sakuraba, K. Hasegawa, M. Mizuguchi, T. Kubota, S. Mizukami, T. Miyazaki, and K. Takanashi, “Anomalous Nernst Effect in L1₀-FePt/MnGa Thermopiles for New Thermoelectric Applications,” *Applied Physics Express*, vol. 6, p. 033003, mar 2013.

- [83] U. Martens, T. Huebner, H. Ulrichs, O. Reimer, T. Kuschel, R. R. Tamming, C.-L. Chang, R. I. Tobey, A. Thomas, M. Münzenberg, and J. Walowski, “Anomalous Nernst effect and three-dimensional temperature gradients in magnetic tunnel junctions,” *Communications Physics*, vol. 1, p. 65, dec 2018.
- [84] T. Kikkawa, K. Uchida, S. Daimon, Y. Shiomi, H. Adachi, Z. Qiu, D. Hou, X.-F. Jin, S. Maekawa, and E. Saitoh, “Separation of longitudinal spin Seebeck effect from anomalous Nernst effect: Determination of origin of transverse thermoelectric voltage in metal/insulator junctions,” *Physical Review B*, vol. 88, p. 214403, dec 2013.
- [85] S. Y. Huang, X. Fan, D. Qu, Y. P. Chen, W. G. Wang, J. Wu, T. Y. Chen, J. Q. Xiao, and C. L. Chien, “Transport Magnetic Proximity Effects in Platinum,” *Physical Review Letters*, vol. 109, p. 107204, sep 2012.
- [86] I. Dzyaloshinsky, “A thermodynamic theory of weak ferromagnetism of antiferromagnetics,” *Journal of Physics and Chemistry of Solids*, vol. 4, pp. 241–255, jan 1958.
- [87] T. Moriya, “Anisotropic Superexchange Interaction and Weak Ferromagnetism,” *Physical Review*, vol. 120, pp. 91–98, oct 1960.
- [88] S. G. Lipson, “The Thermal Hall Effect in Copper,” in *Low Temperature Physics LT9*, pp. 814–817, Boston, MA: Springer US, 1965.
- [89] X. Li, L. Xu, L. Ding, J. Wang, M. Shen, X. Lu, Z. Zhu, and K. Behnia, “Anomalous Nernst and Righi-Leduc Effects in Mn₃Sn : Berry Cur-

- vature and Entropy Flow,” *Physical Review Letters*, vol. 119, p. 056601, aug 2017.
- [90] P. J. Tausch and R. S. Newrock, “High-field Righi-Leduc effect and lattice thermal conductivity of potassium,” *Physical Review B*, vol. 16, pp. 5381–5389, dec 1977.
- [91] Q.-L. Xu, Z.-G. Zhu, and G. Su, “Generalized Fourier law and anomalous RighiLeduc effect in a ferromagnet,” *Physics Letters A*, vol. 382, pp. 3115–3119, oct 2018.
- [92] F. J. Jedema, H. B. Heersche, A. T. Filip, J. J. A. Baselmans, and B. J. Van Wees, “Electrical detection of spin precession in a metallic mesoscopic spin valve,” *Nature*, vol. 416, no. 6882, pp. 713–716, 2002.
- [93] F. L. Bakker, A. Slachter, J.-P. Adam, and B. J. van Wees, “Interplay of Peltier and Seebeck Effects in Nanoscale Nonlocal Spin Valves,” *Physical Review Letters*, vol. 105, p. 136601, sep 2010.
- [94] A. Slachter, F. L. Bakker, and B. J. van Wees, “Anomalous Nernst and anisotropic magnetoresistive heating in a lateral spin valve,” *Physical Review B*, vol. 84, p. 020412, jul 2011.
- [95] S. Hu and T. Kimura, “Anomalous Nernst-Ettingshausen effect in nonlocal spin valve measurement under high-bias current injection,” *Physical Review B*, vol. 87, p. 014424, jan 2013.

Acknowledgement

This thesis would not have been possible without the support of many people.

First of all, I would like to address my sincere gratitude to all the members in the defense committee, Prof. Kimura, Prof. Wada, Prof. Satoh, Prof. Mitsuda and Prof. Matsuyama for the valuable inputs.

I owe my utmost gratitude to Prof. Kimura, my supervisor, for enabling my research activities in a stimulating environment and providing me with ample resources, motivating me with exciting new ideas, giving me financial support and helping me get on with life in Japan. He was always available for discussion. He also took care of my academic and personal growth and introduced me to several researchers in the field during conferences or when they visit our lab.

I would like to thank Prof. Ohnishi who was always the person behind the scenes, keeping every tool running and everything organized and also for being a friendly, comforting presence at any time of the year.

Prof. Ohnishi and Prof. Yamada taught me a lot of things during the teaching assistantship. Speaking of TA, a big thanks to Ohsugi-san because of whom I learnt about the systematic ways of teaching in Japan which I will probably use in future.

I would also like to thank Prof. Ashwin Tulapurkar, my Masters advisor,

who initiated me into research and taught me all the fundamentals. Hu-san, Nomura-san and Yamanoi-san, being the omniscient senpais, had the greatest contribution to my learning experience in the lab. They taught me how to use various tools and how to do systematic research, and had many useful discussions with me. Their theses have always been great reference materials for me. I also had significant help from Ariki-san, Ogawa-san, Kawakita-san, Nakano-san and Uematsu-kun.

A very special thanks to Ishima-san, our secretary, without whom it would have been impossible to live. She was always patiently correcting my mistakes and was always there to count on whenever I needed anything related to office procedures. I would also thank all the office members of the Department of Physics and the Graduate school of Science for their help with various procedures. Particularly, I want to thank Toyoda-san and Ijima-san who were as caring as family and I could walk into the office anytime and ask for information.

All the present and past members of the lab were always good friends with whom I had countless lunchtime conversations and it is them that made me feel at home in the lab. Therefore I thank each and every member of Kimura-laboratory, including Sady-san, Ishitaki-kun, Zaman-bhai, Tasku and Thomas.

I would also like to thank my friends outside the laboratory, especially Beth, Fred, Pradeep, Yogesh, Poornenth, Pritam, Angana, Vijayeta and countless others without whom I would have been lost and lonely at various points of my timeline in Japan.

Last but not the least, I would like to thank my parents and sister for being the supportive family that they have been. Finally, I would like to thank MEXT, Japan for their financial support.